
This is an electronic reprint of the original article.
This reprint may differ from the original in pagination and typographic detail.

Torkan, Masoud; Uotinen, Lauri; Baghbanan, Alireza; Rinne, Mikael

Experimental and numerical characterization of hydro-mechanical properties of rock fractures : The effect of the sample size on roughness and hydraulic aperture

Published in:
International Journal of Rock Mechanics and Mining Sciences

DOI:
[10.1016/j.ijrmms.2024.106009](https://doi.org/10.1016/j.ijrmms.2024.106009)

Published: 01/02/2025

Document Version
Publisher's PDF, also known as Version of record

Published under the following license:
CC BY

Please cite the original version:
Torkan, M., Uotinen, L., Baghbanan, A., & Rinne, M. (2025). Experimental and numerical characterization of hydro-mechanical properties of rock fractures : The effect of the sample size on roughness and hydraulic aperture. *International Journal of Rock Mechanics and Mining Sciences*, 186, Article 106009. <https://doi.org/10.1016/j.ijrmms.2024.106009>

This material is protected by copyright and other intellectual property rights, and duplication or sale of all or part of any of the repository collections is not permitted, except that material may be duplicated by you for your research use or educational purposes in electronic or print form. You must obtain permission for any other use. Electronic or print copies may not be offered, whether for sale or otherwise to anyone who is not an authorised user.



Experimental and numerical characterization of hydro-mechanical properties of rock fractures: The effect of the sample size on roughness and hydraulic aperture

Masoud Torkan^{a,*} , Lauri Uotinen^a , Alireza Baghbanan^b , Mikael Rinne^a 

^a Department of Civil Engineering, School of Engineering, Aalto University, Espoo, Finland

^b Department of Mining Engineering, Isfahan University of Technology, Isfahan, Iran

ARTICLE INFO

Keywords:

Photogrammetry
Physical aperture
Roughness
Experimental and numerical tests
Hydraulic aperture
Scale effect

ABSTRACT

This paper investigated fluid flow in low-stress conditions through rock fractures in Kuru granite measuring 25 cm × 25 cm. Physical aperture and roughness were measured using high-precision photogrammetry. Anisotropy in roughness was observed in two perpendicular directions. Physical aperture under normal stresses was measured, and fracture closure was compared with linear variable displacement transducer (LVDT) measurements, showing good agreement. Hydromechanical tests exhibited nonlinear behavior between fluid pressure gradient and flow rate, following the Forchheimer equation. Applying normal stress resulted in decreased hydraulic aperture and increased nonlinearity of fluid flow. Experimental hydromechanical tests also revealed anisotropy in perpendicular directions, aligning with fracture roughness measurements. Photogrammetric models, aided COMSOL simulations, closely matched the experimental results. Increased stress induced channeled flow and greater tortuosity. Validation of the numerical model allowed simulations on larger fractures. A 2 m × 1 m granite fracture studied scale effects, with the rough surface duplicated and shifted by 350 μm to align with initial aperture measurements of 25 cm × 25 cm samples. Fluid flow simulations assessed subsample sizes (5 cm–100 cm), showing size-dependent variations in roughness, hydraulic aperture, and non-Darcy coefficient, stabilizing beyond 30 cm. This underscores sample size's role in parameter stabilization beyond a 30 cm scale.

1. Introduction

Rock engineering projects, such as underground excavations, rock slopes, or mining operations, can disturb the stress distribution in the rock mass. This redistribution can lead to the opening, closing, shearing, or dilation of pre-existing fractures and may also initiate new fractures. These changes can increase the deformability and permeability of the rock mass. The interaction between hydraulic and mechanical processes, known as hydro-mechanical coupling, can further affect effective stress, including fluid pressure and flux. Accurate estimation of hydro-mechanical properties is critical for predicting flow paths and discharge rates in a rock mass.

A fractured rock mass is a complex material composed of intact rock, fracture systems, and possible infillings.¹ The inhomogeneous nature of rock complicates the modeling of hydro-mechanical processes. In crystalline and metamorphic rocks, most water flow occurs through the fracture system, and the permeability of intact rock can be considered

negligible.^{2–4} The behavior of each fracture is controlled by its geometrical properties (aperture, length, and roughness) and mechanical properties (stiffness and closure), which greatly influence the overall hydro-mechanical properties.^{3,5,6} A wide range of factors, such as aperture, roughness, contact area, stress state, matedness, scale effects, and fluid rheology, influence fracture permeability.⁷

Fracture aperture can be described by wall roughness, void spaces, and contact areas.⁵ Physical and hydraulic apertures, which describe theoretical and experimental permeability, are usually not identical. Hydraulic aperture is often smaller than physical aperture. Extensive research has established several relationships between hydraulic and physical apertures based on fracture geometries, summarized in prior studies.^{8,9}

Fracture aperture can be measured by both contact and non-contact methods. Scanning the fracture surface topography with photogrammetry is one example of a non-contact method.^{10,11} Aperture can also be measured by X-ray CT techniques,¹² laser scanning,¹³ and

* Corresponding author.

E-mail address: masoud.torkan@aalto.fi (M. Torkan).

<https://doi.org/10.1016/j.ijmms.2024.106009>

Received 23 August 2024; Received in revised form 29 October 2024; Accepted 21 December 2024

Available online 30 December 2024

1365-1609/© 2024 The Author(s). Published by Elsevier Ltd. This is an open access article under the CC BY license (<http://creativecommons.org/licenses/by/4.0/>).

photogrammetry techniques.¹⁴ Contact measurement techniques, such as injection⁵ and casting,¹⁵ are also applicable for measuring apertures. Non-contact methods can involve back-calculation hydraulic tests in the laboratory,¹⁶ numerical modeling,¹⁷ and in-situ scale tests.^{18,19} Fracture surface roughness is mainly influenced by size, shape, arrangement, and fluctuation of asperities. Fracture surface roughness is influenced by the size, shape, arrangement, and fluctuation of asperities. Additionally, roughness can be affected by sample size due to roughness wavelength.⁹ Both contact approaches like profilometry²⁰ and non-contact methods such as photogrammetry¹⁴ can be used to estimate roughness. Surface roughness is often naturally anisotropic, which may lead to anisotropic hydro-mechanical properties due to paleo stress history and mechanical loading.

Fluid flow behavior in a single fracture may follow the cubic law, which is a simplified solution to the Navier-Stokes equations.¹⁶ The cubic law suggests a relationship between permeability and hydraulic aperture, for any given fluid flow following Darcy's law.¹⁶ In this formulation, a single fracture is modeled as two smooth and parallel plate media, neglecting the effects of surface roughness and aperture variation. Surface roughness and contact areas can introduce tortuosity and flow cavitation, resulting in discrepancies between observed flow rates and measured apertures.²¹ Moreover, Darcy's law is applicable primarily for low flow velocity regimes.^{22,23} In addition, changes in fluid pressure can lead to nonlinearity, indicating that Darcy's law may not estimate flow rates accurately in rough fractures.^{24,25} It means a non-linear behavior tends to happen and Darcy's law cannot be used to estimate flow rate in rough fractures. To address this issue, several studies have improved the cubic law by considering roughness,^{26–28} contact areas,^{29–31} and aperture.^{32,33}

Forchheimer equation³⁴ and Izbash equation³⁵ are well-known relationships that can account for the nonlinear deviations between pressure gradients and flow rates in rough fractures. Both equations, Forchheimer and Izbash, could model the non-linear behavior of flow similarly.^{36,37} Coefficients for the Forchheimer equation have been evaluated under various confinement and normal stress conditions.^{38–40} Nonlinear flow tests have been conducted through matching and mismatching 3D-printed fractures⁴¹ and real rough fractures⁴² based on fractal theory. The Forchheimer equation's coefficients were influenced by roughness and aperture.

The effect of normal stress on the permeability of rock fractures has been studied by several researchers.^{9,40} The findings indicate that increasing normal stress can reduce aperture and increase contact areas.^{40,43} Anisotropy can introduce variations in fluid flow behavior along different pressure gradient directions through the same fracture, resulting in varying outcomes.⁴⁴ Factors such as shear direction,^{17,45} sample size,^{17,46} and aperture^{47,48} could contribute to anisotropy in fluid flow behavior.

Large laboratory-scale experiments are often costly, time-consuming, and complicated.⁴ Consequently, numerical modeling has been used to investigate stress and scale effects on fracture permeability. Numerical simulation is crucial for studying fluid flow behavior through a single fracture under varying normal and shear stresses.^{43,49} Different approaches have been used to simulate fluid flow through fractures, for example, 2D,¹⁷ quasi 3D,^{50,51} and 3D models,^{43,48} real⁴³ or hypothetical^{50,52} fractures, utilizing flow models such as Navier-Stokes⁴³ or Reynolds equations.⁴⁹ Limitations exist in 2D fracture models, as they simplify 3D models and ignore transverse flow and the flow regime in the third dimension (z-axis). This simplification results in an incomplete incorporation of geometry changes caused by mechanical, geochemical, and thermal processes, as well as neglecting roughness and vertical tortuosity. To overcome these limitations, 3D models are preferred. However, hypothetical fractures generated through artificial methods may lead to overestimations or underestimations compared to real 3D models. Additionally, simplifying Navier-Stokes equations into Reynolds equations may yield inaccurate results.

Scale effects on fracture permeability are less frequently discussed,

with few researchers have addressed this issue.^{21,43,50,52–60} Accurate interpretation of results may be challenging due to the scarcity of studies on scale effects on fracture permeability. However, there is no unanimous agreement on whether hydraulic conductivity increases or decreases with increasing fracture size. Furthermore, several scholars have examined the scale effect on permeability concerning stress dependency.^{21,53}

To summarize, numerous studies have explored numerical modeling and laboratory-scale experiments. For example, a numerical study suggests that smaller fractures exhibit lower hydraulic conductivity than larger ones under the same normal stress due to the absence of continuous fluid flow channels.⁵⁴ Large-scale roughness can significantly influence the hydraulic and mechanical properties of a fracture. As a result, smaller samples below a certain size may not provide an accurate representation of the overall hydraulic and mechanical behavior of the fracture.⁵⁵

Fractures with a constant mean aperture showed negligible variations in hydraulic aperture beyond a fracture size of approximately 20 cm, as the standard deviation of the initial aperture became independent of fracture size.⁵⁷ The influence of scale effects diminished for normal stresses exceeding 25 MPa.⁵⁸ Simulations of various scales, ranging from 1/15 to 1, extracted from a 50 mm × 100 mm fracture, demonstrated that the transmissivity of the fracture was independent of scale. The 1/9 scale simulation of the fracture adequately represented the entire rock fracture, providing a reasonable basis for comparison with experimental test outcomes.⁴³

To achieve constant hydraulic conductivity and determine a representative sample size, the mean aperture, roughness, and normal stress of the fracture were numerically analyzed using rough fractures in both square shape⁵⁰ and radial shape forms.⁵² Validation of these numerical models involved conducting fluid flow tests on fabricated samples of varying sizes (5, 10, and 15 cm). The numerical simulations of rough fractures highlighted the dependency of hydraulic properties and roughness on sample size. In this specific study, laboratory sample sizes of 1 m × 1 m were found inadequate to represent field-scale fractures. By upscaling the samples to 20 m × 20 m and performing numerical modeling of fluid flow, it was shown that the representative size exceeded 2 m.⁶⁰ An investigation into surface roughness showed that roughness stabilized once fracture sizes reached a critical range of 300–400 mm. Additionally, numerical modeling demonstrated a similar stabilization trend in permeability for fractures within this critical size range.⁴⁶

Despite existing experimental and numerical research at laboratory scales, the stress dependency of roughness and permeability remains unclear. This study aims to utilize photogrammetry to characterize rough surfaces and measure physical aperture under varying normal stresses, as well as to employ photogrammetric 3D models for numerical simulations of fluid flow through fractures. To achieve this, a series of laboratory experiments were conducted to measure the permeability of rock fractures under different levels of normal stress and water pressure gradients. To assess anisotropy, roughness, and permeability were measured in perpendicular directions. Three homogeneous grey Kuru granite samples with dimensions of 25 cm × 25 cm × 10 cm and featuring a single rough fracture were used in the experiments. 3D models of the fracture between the two rock slabs were reconstructed using photogrammetry to evaluate physical apertures and roughness under varying normal stresses. These models provided a basis for calculating aperture and estimating permeability.

The 3D point clouds reconstructed from photogrammetry were also used to regenerate accurate 3D models of the fractures for numerical simulations in COMSOL. The Navier-Stokes equation was employed to simulate fluid flow through the fractures, assessing the impact of different water pressure gradients as physical apertures decreased under varying normal stresses.

Additionally, the study examined the effects of sample size on the roughness and hydraulic apertures of rock fractures. Numerical 3D

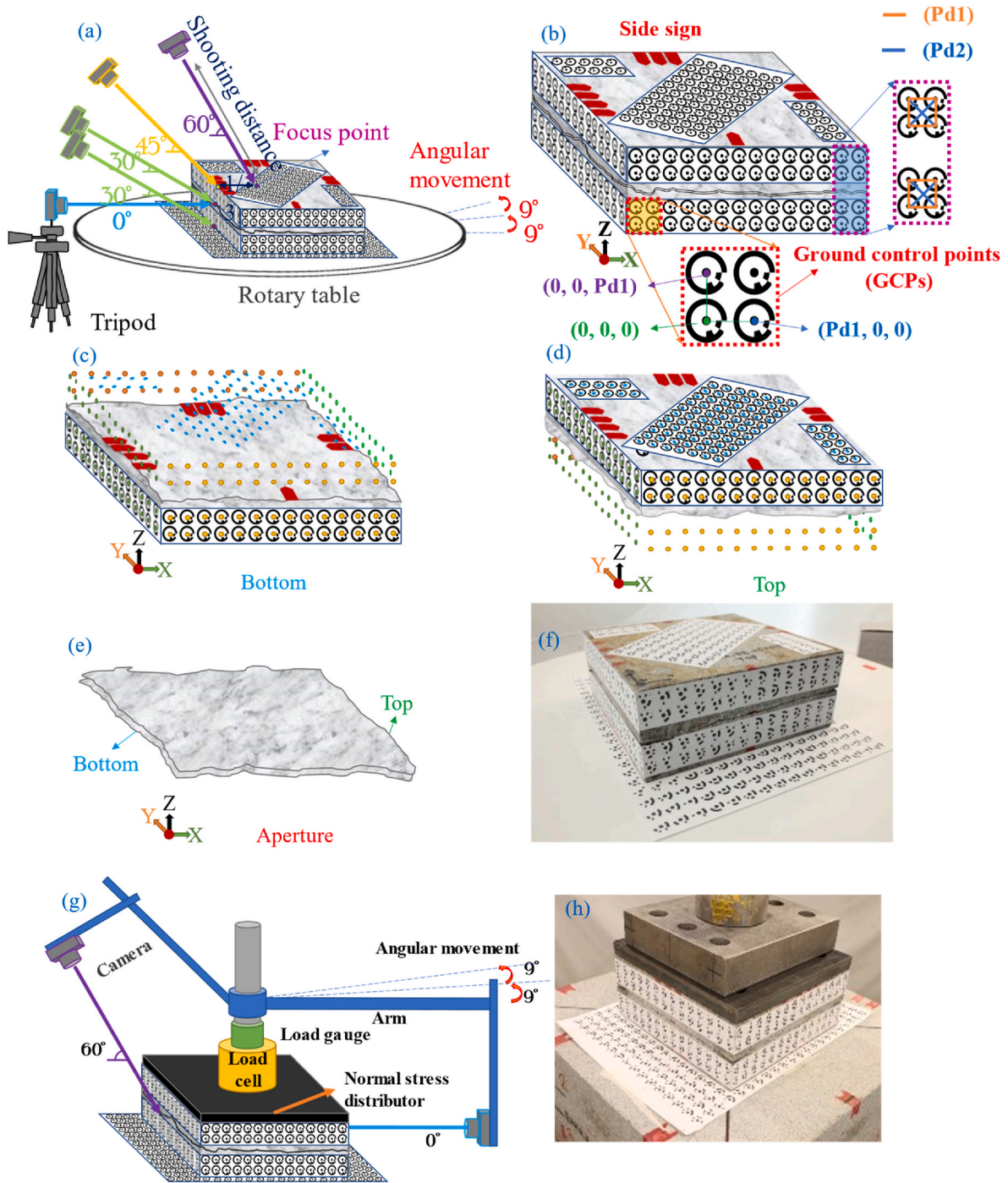


Fig. 1. Photogrammetry and measurement procedures for fracture morphologies, (a) a method used to photograph the entire sample, top and bottom halves covered by predefined markers, (b) establishing a coordinate system, performing scaling and orientation, and extracting the coordinate data of markers, (c and d) aligning each half in the same coordinate system, (e) measuring physical aperture, (f) Sample 3 was photographed at a pitch angle of 30°, (g) detecting displacement while applying normal stress by photogrammetry; and (h) the photo of Sample 1 under normal stress 0.1 MPa photographed at a pitch angle of 60°, modified after ⁶⁵.

models were utilized to extract cross-sectional areas, and fluid flow through these areas was analyzed to assess the scale effect. To understand the influence of scale, the photogrammetric 3D models of a 2 m × 1 m Kuru granite sample were selected and divided into three 1 m × 1 m subsamples. Further subsamples, ranging from 5 cm × 5 cm to 100 cm × 100 cm, were extracted to measure roughness, and numerical modeling was conducted to study scale effect on fluid flow behavior and calculate hydraulic aperture and the non-Darcy coefficient.

The innovation of this paper lies in the use of high-accuracy photogrammetry as a powerful tool for modeling physical aperture and

measuring roughness. This method allows for precise assessment of changes in physical aperture under normal stress, leading to fluid flow simulations that closely match experimental models. Photogrammetry detects changes in the entire physical aperture rather than just the average from LVDTs, enabling more accurate modeling. The study aims to enhance understanding of fluid flow behavior and investigate the scale effect on linear and nonlinear coefficients of the Forchheimer equation using 3D photogrammetric models.

Table 1
Calibrated values of distortion model for the DSLR camera.⁶⁵

Parameters	Focal length (mm)	Principal point x (mm)	Principal point y (mm)	Radial 1	Radial 2	Radial 3	Tangential 1	Tangential 2
Calibrated values	35.120300	0.000000	-0.016992	-0.048229	0.126181	-0.160469	0.000045	0.000405

2. Materials and methods

2.1. Specimen preparation

Kuru grey rock blocks were split into two halves using mechanical splitting. The plug and feather technique was employed to propagate a tensile fracture. In this method, a series of holes were drilled along the splitting line, where alternating plug and feather wedges were inserted and struck with a hammer to induce tensile stress. This process resulted in a controlled planar tensile fracture. Before splitting, the rock blocks were inspected to identify pre-existing defects and determine the drilling directions for the holes. After splitting, the area around the plug and feather wedges was removed, and the remaining rock block was cut into the intended dimensions of 25 cm (width) × 25 cm (length) × 10 cm (height).

2.2. Characterization of geometrical properties of fractures

2.2.1. Photography procedure and data acquisition

The Structure-from-Motion Multi-View Stereo (SFM-MVS) photogrammetric method was employed to assess the physical aperture and roughness of fractures (Fig. 1). SFM-MVS photogrammetry utilizes multiple overlapping 2D images to generate a 3D model.^{61,62} A calibrated Canon 5DS R DSLR camera with a Canon 35 mm f/1.4L II USM lens was used for image capture, and the calibrated values of the camera, based on the Brown 3 with tangential 2 distortion model, are shown in Table 1. An illuminance level of 4000 lx was provided to ensure adequate lighting for indoor photogrammetry.

To scale and orient the 3D photogrammetric models, 12-bit circular-coded markers were used (Fig. 1b). These markers were automatically recognized by RealityCapture V1.2.1 software.⁶³ The markers were printed on sticker sheets with predefined distances of 17950 μm (center-to-center vertically and horizontally) and a resolution of 1200 DPI. The distance between the markers was measured digitally using GIMP software⁶⁴ with an accuracy of 1 μm. The predefined distances helped to minimize errors that could occur with manual measurements. Two specific distances were defined: Pd1 (17950 μm) center-to-center vertically and horizontally, and Pd2 (25385 μm) center-to-center diagonally (Fig. 1b).

For scanning, each sample was placed on a rotary table, and 40 images were taken for every 9° of rotation (Fig. 1a). The scanning process was conducted at four distinct angles: 0°, 30°, 45°, and 60° (Fig. 1a). At 30°, two different focal points were used to capture additional details from the marker positions on the sample. To obtain more accurate data from rough surfaces, an additional angle of 75° was used for each half. The sample halves were then flipped, and the process was repeated at angles of 30°, 45°, and 60°. For samples under normal stresses, photography was conducted at pitch angles of 0° and 60°, with 9° angular movements (Fig. 1g). The images were subsequently imported into RealityCapture to reconstruct the 3D models. The 'Brown 3 with tangential 2' distortion model was selected for component alignment (Table 1) and to correct photo distortion.

2.2.2. Measuring physical aperture by photogrammetry

To calculate the physical aperture, it was necessary to align the two halves of each sample within the same coordinate system.⁶⁵ Three Ground Control Points (GCPs) were used (Fig. 1b), providing a position accuracy of 1 μm. This step facilitated the alignment of the 3D models within a specific coordinate system. Scale bars (Pd1 and Pd2) were defined between the markers to ensure well-matched 3D models in the

software, allowing for realignment of the models to adjust scaling and marker positions. Coordinate data for the markers were exported from the 3D well-matched models at each normal stress level (0, 0.1, 0.3, and 0.5 MPa). These low normal stresses allowed to detect changes that occurred only in the physical aperture, without affecting the fracture surface or causing any damage to surfaces. For example, Fig. 1f and h show Sample 3 and Sample 1 under normal stresses of 0 and 0.1 MPa, respectively. These data were then used to measure physical aperture under varying normal stresses (Fig. 1c, d, and 1e). CloudCompare software 2.12.4⁶⁶ was then used to calculate physical aperture distributions. The 3D rough surfaces of the fractures were extracted, and the cloud-to-cloud distance tool in CloudCompare was employed to compute the distance between the top and bottom surfaces along the Z direction (Fig. 1e). Values were considered as physical aperture, while negative and zero values were treated as contact areas.

Both photogrammetry and linear variable displacement transducers (LVDTs) were used to measure deviations in physical aperture under varying normal stresses. The results from both methods were compared to validate the photogrammetric data for numerical simulations. It was assumed that only fracture closure occurred due to the low levels of normal stress, with no rock deformation observed. The full process of photogrammetry and physical aperture measurement is detailed in previous research.⁶⁵

2.2.3. Measuring roughness by photogrammetry

The Joint Roughness Coefficient (JRC) is a widely used method for quantifying surface roughness. It is estimated by comparing extracted profiles from fracture surfaces with ten standard profiles.²⁰ In this study, photogrammetric 3D models of rough rock surfaces were used to estimate roughness and JRC. The process involved rasterizing 3D point clouds of rock surfaces with a resolution of 0.5 mm × 0.5 mm. Following this, profiles were extracted from the rasterized point clouds at a 0.5 mm sampling interval, with distances of 0.5 mm between each profile. This was done for both the top and bottom surfaces in the X and Y directions, allowing for a systematic analysis of surface roughness estimation.

Various formulas have been proposed to quantify the geometry of roughness and establish relationships between roughness parameters and JRC values.⁶⁷ For instance, the roughness parameter Z_2 (Eq. (1)), proposed by Myres in 1962⁶⁸, represents the Root Mean Square (RMS) of the local slope of the profile. This parameter (Z_2) was analyzed using different sampling intervals to establish a correlation with JRC. For example, JRC for a 0.5 mm interval was estimated using the formula presented in Eq. 3:⁶⁹

$$Z_2 = \sqrt{\frac{\sum_{i=1}^{n-1} (z_i - z_{i+1})^2}{(n-1)(\Delta x)^2}} \quad \text{Eq. 1}$$

Where Z_2 denotes Root Mean Square of the first derivative of the asperities, z_i signifies the height at sampling point i , n represents the number of samples, and Δx is the interval between samplings. Z_{2k} signifies the roughness in the k -th fracture profile, and \bar{Z}_2 is the average of Z_{2k} for the certain number of profiles (m) in each direction of each surface (Eq. (2))

$$\bar{Z}_2 = \frac{1}{m} \sum_{k=1}^m Z_{2k} \quad \text{Eq. 2}$$

The JRC_k value for the k -th fracture profile is calculated by Eq. (3):

$$JRC_k = 61.79(Z_2) - 3.47 \quad \text{Eq. 3}$$

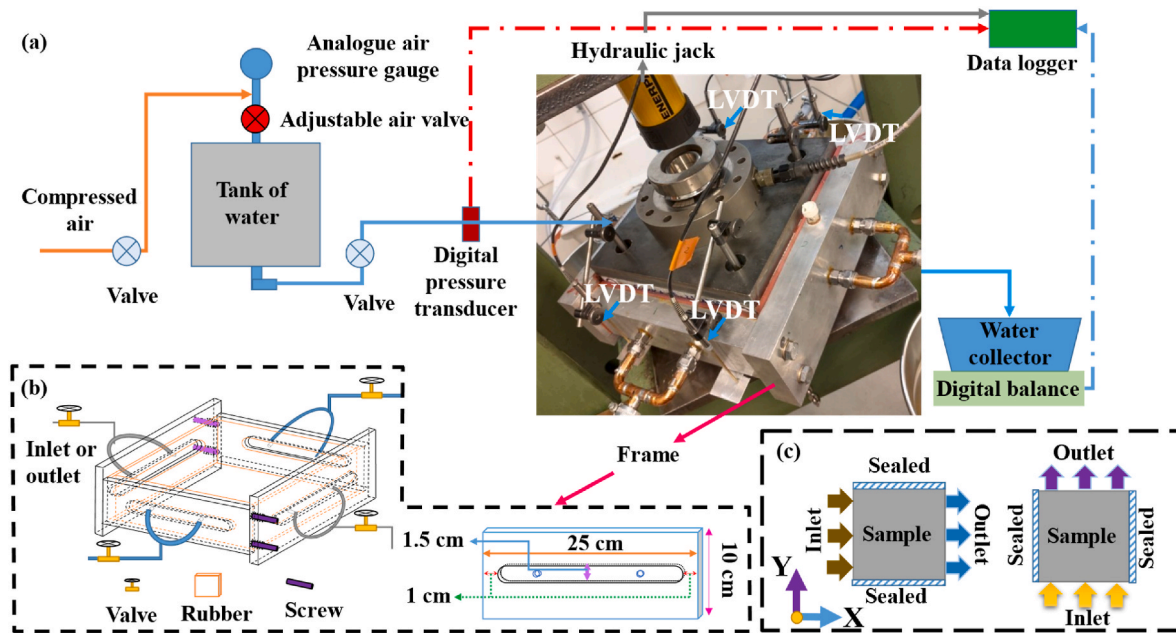


Fig. 2. (a) The experimental setup for indicating the functioning principle of water flow test and LVDTs' positions around a sample, (b) the self-designed frame and interior faces' dimensions of the frames,⁷² and (c) schemes of hydraulic boundary conditions.

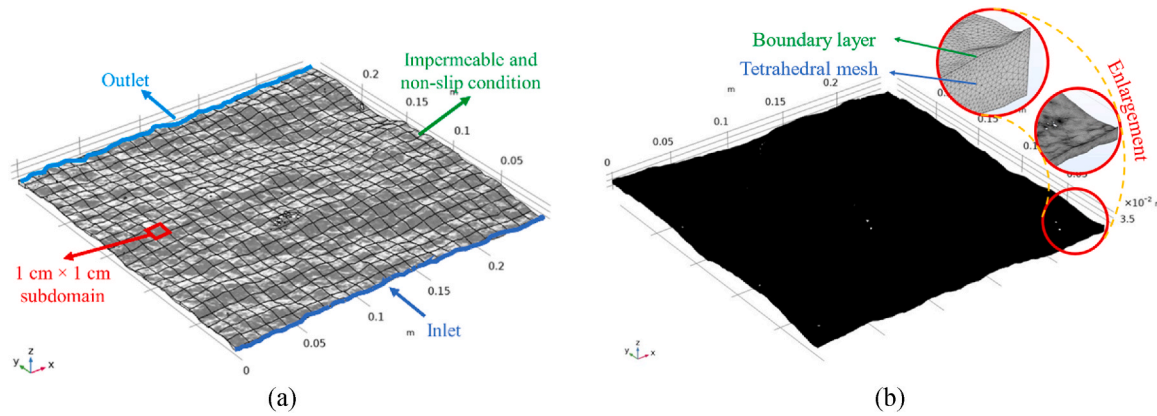


Fig. 3. Boundary conditions of flow simulation in each direction, (a) preparation for meshing and (b) a meshed model.

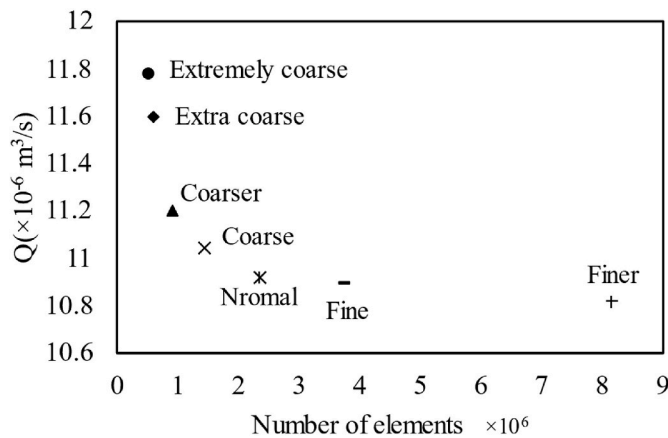


Fig. 4. Mesh analysis for different element sizes.

The JRC_k values obtained for each profile in both directions on the top and bottom surfaces are averaged to calculate the overall JRC value for each direction using Eq. (4):

$$JRC = \frac{1}{m} \sum_{k=1}^m JRC_k \quad \text{Eq. 4}$$

This comprehensive assessment of roughness in different directions facilitates the analysis of anisotropy.

2.3. Theoretical background

The fluid flow through a fracture is governed by Navier-Stokes (N-S) equations,² represented by Eq (5):

$$\frac{\partial u}{\partial t} + (u \cdot \nabla)u = F - \frac{1}{\rho} \nabla p + \frac{\mu}{\rho} \nabla^2 u \quad \text{Eq. 5}$$

Where u is the flow velocity (m/s), t is time (s), F is the body force, ρ is the fluid density (kg/m³), μ is the fluid viscosity (Pa.s), and ∇p is the pressure gradient (Pa/m). The body force is due to gravity in most situations. The continuity equation (Eq. (6)), which expresses the

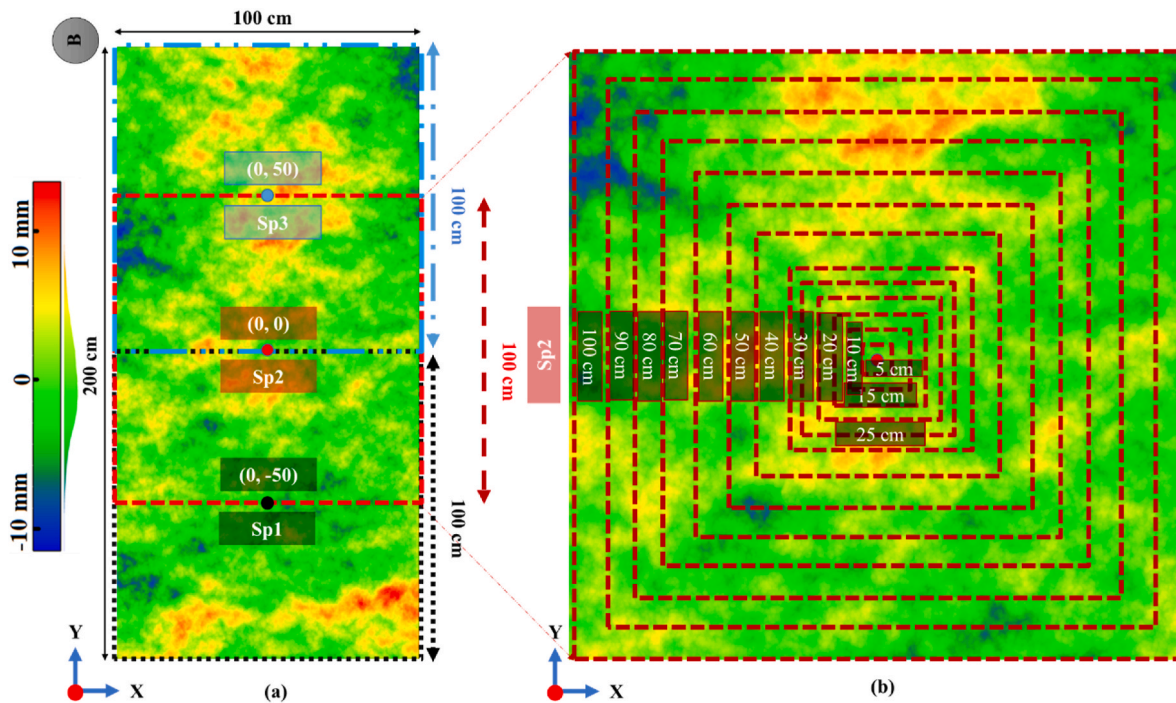


Fig. 5. (a) The 2 m × 1 m rough surface (modified after⁷⁴) and three 1 m × 1 m sample sizes extracted from, and (b) the subsamples extracted from 1 m × 1 m rough surfaces for numerical simulations. The histogram shows the height distribution of asperities.

conservation of mass, is incorporated to complete the closed system of equations for an incompressible fluid:

$$\nabla \cdot u = 0 \tag{Eq. 6}$$

The gravitational term can be dropped out from the equation by introducing equation $P = p + \rho gh$ to Eq. (5) and the time-dependent term $(\partial u / \partial t)$ can be ignored by steady state assumption (Eq. (7)).

$$\rho(u \cdot \nabla)u + \nabla P = \mu \nabla^2 u \tag{Eq. 7}$$

Where $\rho(u \cdot \nabla) u$ represents the inertial forces and $\mu \nabla^2 u$ represents the viscous forces. When the viscous forces are dominant over inertial forces, the Navier-Stokes equations can be linearized into the Stokes equations (Eq. (8)) which are appropriate for modeling fluid flows with low Reynolds numbers in regular geometries.

$$\mu \nabla^2 u - \nabla P = 0 \tag{Eq. 8}$$

In cases where the viscous forces dominate the inertial forces and the aperture variation is gradual, the N-S equations are further simplified into the Reynolds equation, represented by equation (Eq. (9)):

$$\nabla \cdot (e^3 \nabla P) = 0 \tag{Eq. 9}$$

Where e signifies the aperture. The cubic law, simplified Navier-Stoke equations, is used to describe fluid flow through an open fracture whose sides are parallel and smooth when the flow is laminar,³³ as shown in Eq. (10):

$$Q = - \frac{\Delta P}{L \mu} \frac{w e_h^3}{12} \tag{Eq. 10}$$

Where Q denotes the volumetric flow rate (m^3/s), ΔP is the pressure difference between the inlet and the outlet (Pa), w is the width of the fracture (m), e_h signifies the hydraulic (equivalent) fracture (m), μ is the dynamic viscosity of water (Pa.s), L represents the length of the fracture (m).

Differentiating between laminar flow and turbulent flow is crucial to understanding the fluid flow mechanism through a fracture. This difference is determined by the Reynolds number. It is a dimensionless

number, which is defined as the ratio of inertial forces to viscous forces and expressed with Eq. (11):

$$Re = \frac{\rho Q}{\mu w} \tag{Eq. 11}$$

Where ρ is the fluid density (kg/m^3), Q denotes flow rate (m^3/s), μ signifies the dynamic viscosity of water (Pa.s) and w represents the width of the fracture (m). There are some disagreements about the Reynolds number's transition in laminar to nonlaminar flow regimes, that is the flow difference between a rough fracture and a smooth one.³⁶ The critical Reynolds number for practical purposes is 10.⁷⁰ Using the cubic law with a high Reynolds number may overestimate the flow rate for a rough fracture.^{2,36} To address this issue, employing Forchheimer equation (Eqs. (12)–(15)) could help to describe the nonlinear flow in rough fractures.⁷⁰ The validity of this equation has been confirmed through various aspects such as experiments, numerical modeling, and theoretical analyses.^{36,37,70,71}

$$-\nabla P = A Q + B Q^2 \tag{Eq. 12}$$

$$-\nabla P = \frac{\Delta P}{L} \tag{Eq. 13}$$

$$A = \frac{12 \mu}{w e_h^3} \tag{Eq. 14}$$

$$B = \frac{\beta \rho}{w^2 e_h^2} \tag{Eq. 15}$$

Where ∇P is the pressure gradient (Pa/m), A (kg/sm^5) and B (kg/m^8) denote two coefficients of Forchheimer equation describing pressure drop components caused by linear and nonlinear effects, respectively, β (m^{-1}) is called the non-Darcy coefficient and shows inertial effect. If the non-Darcy coefficient ($\beta = 0$) is neglected or equals zero, Eq. (7) reduces to Darcy's law (Eq. (5)). This means Forchheimer equation can be used to characterize Darcy flow and non-Darcy flow in rough fractures. Therefore, two parameters in Forchheimer equation should be found, hydraulic aperture (e_h) and the non-Darcy coefficient (β).

Table 2
Physical aperture and comparison between results of LVDTs and photogrammetry.⁶⁵

Sample	1					2					3					
	Average movements of LVDTs (µm)	Photogrammetric movements (µm)	Physical aperture (µm)	Standard deviation of physical aperture (µm)	Average movements of LVDTs (µm)	Photogrammetric movements (µm)	Physical aperture (µm)	Standard deviation of physical aperture (µm)	Average movements of LVDTs (µm)	Photogrammetric movements (µm)	Physical aperture (µm)	Standard deviation of physical aperture (µm)	Average movements of LVDTs (µm)	Photogrammetric movements (µm)	Physical aperture (µm)	Standard deviation of physical aperture (µm)
0	N/A	N/A	366	405	N/A	N/A	330	350	N/A	N/A	314	244	N/A	N/A	314	244
0.1	22	19	347	410	16	12	318	344	23	31	283	208	31	31	283	208
0.3	34	35	331	407	31	38	292	342	50	55	259	208	55	55	259	208
0.5	40	43	323	407	41	49	281	343	65	67	247	206	67	67	247	206

2.4. Experimental setup

To conduct flow-stress experiments on rough rock fractures, a test setup was developed, as shown in Fig. 2. The setup included a frame, a data logger for recording data, a hydraulic jack to apply normal pressure to the samples, a rigid plate to evenly distribute the pressure on the top surfaces, a digital pressure transducer with a resolution of 0.1 kPa for measuring inlet water pressure, a water tank for water supply, and compressed air with an adjustable air regulator to maintain constant inlet pressure (Fig. 2a).

The frame was constructed with four sides and featured a fracture sealing system. Each interior face had a water channel to ensure smooth pressure distribution behind the fractures (Fig. 2b). Rubber seals on the interior sides of the frame prevented leaks, while valves controlled the inlets and outlets to direct water flow. This design enabled the investigation of anisotropic effects on fluid flow in different directions (Fig. 2c). By sealing opposite sides of the setup, fluid flow could be directed through a specific orientation. For instance, when the fracture was sealed in the Y direction, fluid flow occurred only through the X direction (Fig. 2c). Four LVDTs were installed around the sample to measure vertical movements of the fracture after normal stress was applied (Fig. 2a).

Silicone glue and tape were used to seal the sample corners, preventing connections between the sides. During each test, a constant water pressure was applied to one side of the fracture as the inlet pressure (Fig. 2c). Ten water pressures, ranging from 5 kPa to 50 kPa in 5 kPa intervals, were used for testing, with the outlet pressure assumed to be zero. This method also allowed for permeability calculations under normal stress. A digital balance with a precision of 0.001 g was used to measure the outlet water volume. To achieve steady-state conditions, water flow was monitored before measuring the weight to calculate flow rate, ensuring that fluid flow remained consistent with no fluctuations. The system was assembled using 10 mm diameter pipes with smooth inner walls. A hydraulic jack with a control unit applied normal stresses of 0.1, 0.3, and 0.5 MPa with 99 % accuracy.

The experimental tests were conducted in the Department of Civil Engineering laboratory at Aalto University, Espoo, Finland. The temperature during the tests was maintained at 25 °C, with the density and dynamic viscosity of water being $\rho = 0.997 \times 10^3 \text{ kg/m}^3$ and $\mu = 0.89 \times 10^{-3} \text{ Pa s}$, respectively. A total of 240 fluid flow tests were performed under the conditions described.

2.5. Numerical setup and verification

The 3D high-precision photogrammetric point clouds of the top and bottom rough surfaces under varying normal stresses were imported into COMSOL software version 6.1⁷³ to investigate fluid flow through a fracture in steady-state conditions. A parameterized surface function was employed to construct the fracture surfaces. To ensure a uniform mesh and enhance simulation results, the Partition Objects operation was used to subdivide the parametric surfaces into smaller domains, each measuring 1 cm × 1 cm. This size was selected to ensure adequate mesh resolution (Fig. 3a).

The Boolean function in COMSOL was utilized to remove contact areas where the two parametric surfaces intersected. Mesh control domains were applied to accurately refine the mesh in targeted areas of the geometry while leaving the rest of the model unaffected for physics assignment. This approach allowed for precise simulation results by focusing on areas of interest without compromising the overall geometry. For complex geometries such as rough fractures, tetrahedral elements provided a flexible and adaptable mesh suitable for small apertures and contact areas. A boundary layer was applied to the walls of the fractures, which is effective in resolving thin boundary layers along non-slip boundaries in fluid flow problems (Fig. 3b).⁷³

Different water pressures were applied to the inlets for each condition, with the outlet pressure set to zero pascal. The top and bottom

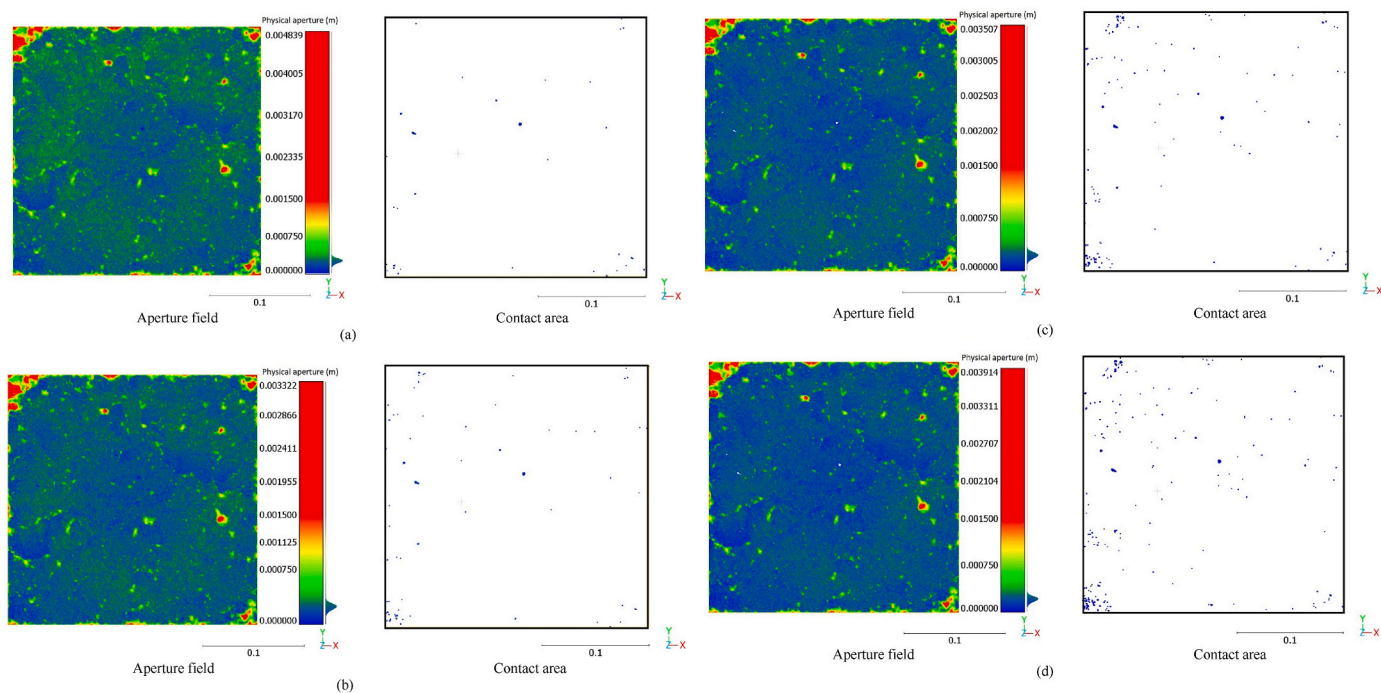


Fig. 6. The photogrammetric physical aperture fields and contact areas of Sample 3 in each normal stress state (a) without normal stress, (b) 0.1 MPa, (c) 0.3 MPa, and (d) 0.5 MPa. The color scales beside the figures show the opening of the apertures, and the histograms illustrate the aperture distribution. (For interpretation of the references to color in this figure legend, the reader is referred to the Web version of this article.)

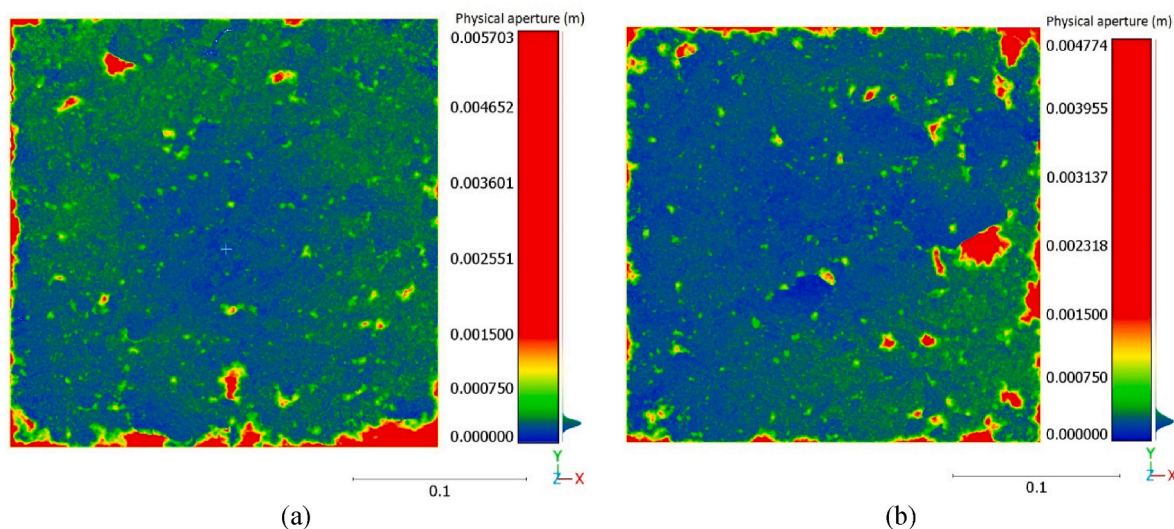


Fig. 7. The photogrammetric physical aperture fields of (a) Sample 1 and (b) Sample 2 without normal stress.

fracture surfaces, along with the side boundaries, were designated as impermeable and non-slip boundaries (Fig. 3a). The outlet flow rate was calculated for each water pressure to determine the relationship between flow rate and pressure gradient of the fractures under varying normal stresses. To verify the numerical modeling against experimental data, the calculated numerical flow rates were compared to the experimental flow rates at different stress levels.

To eliminate the effect of mesh size on the results, a mesh sensitivity analysis was conducted. In this analysis, simulations were performed with various element sizes defined by COMSOL, ranging from Extremely Coarse to Fine mesh sizes, for Sample 2 (at a water pressure of 10 kPa in the X direction and a stress state of 0.1 MPa). The calculated flow rates for different mesh sizes are illustrated in Fig. 4. As shown, the flow rate

variation stabilizes at a Normal element size with a total of 2,300,000 elements, where the deviation becomes negligible (Fig. 4). Fluid flow simulations were subsequently conducted using a Fine element size of approximately 3,700,000 elements, which is one level finer than the Normal size. This choice was made to ensure that if small features emerged, they would not significantly affect the results. The Fine mesh size allows for greater accuracy while still maintaining reasonable computation time, especially since the differences in flow rates between the Normal and Fine sizes were minimal.

2.6. Scale effect

To comprehensively analyze the effect of sample size on

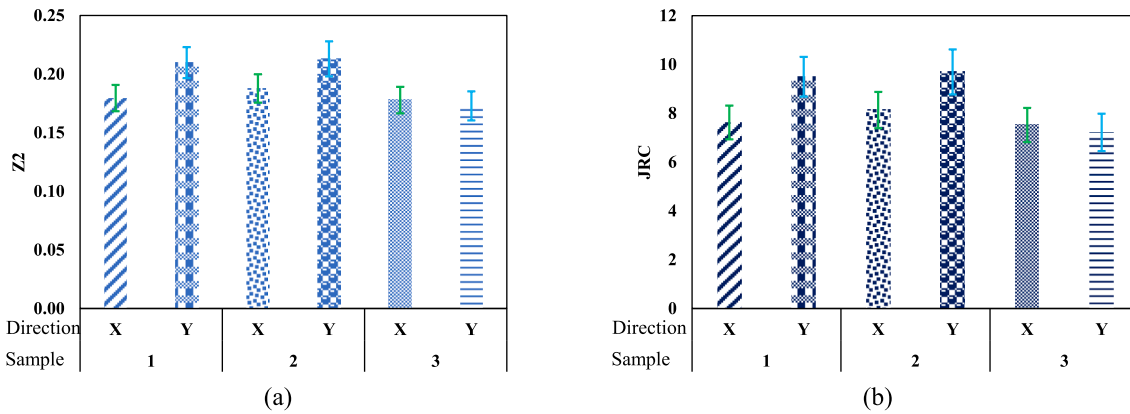


Fig. 8. Mean (a) roughness (\bar{Z}_2) and (b) JRC values, along with their standard deviations, for Samples 1, 2, and 3 in the directions X and Y. The confidence interval, calculated as one standard deviation, is represented by the error bars.

permeability, the 3D point cloud of a 2 m × 1 m rough surface (Fig. 5a) from a previous shear test conducted by⁷⁴ was selected. This 3D point cloud was created using the same material and manufacturing method as in the current study. The photogrammetry technique outlined in prior research⁷⁴ was employed to obtain the 3D point cloud. The bottom surface was duplicated and shifted 350 μm along the Z-axis, corresponding to the physical aperture of the initial samples used in real fluid flow tests without normal stress. The sample was divided into three 1 m × 1 m sections (Sp1, Sp2, Sp3), as illustrated in Fig. 5a. Square subsamples measuring 5, 10, 15, 20, 25, 30, 40, 50, 60, 70, 80, 90, and 100 cm were extracted from each section (Fig. 5b). Roughness was calculated for each subsample to investigate the scale effect. Simulations of fluid flow through these subsamples were conducted using pressure gradients ranging from 20 to 100 kPa/m, with intervals of 20 kPa/m, in both the X and Y directions. To optimize computational efficiency, the 1 m square samples were subdivided into 5 cm × 5 cm subdomains, similar to the meshing method used for Samples 1 to 3. Normal element sizes were selected for the simulations, as there were no contact areas or small apertures involved. The number of mesh elements varied significantly, ranging from approximately 90,000 for the 5 cm × 5 cm subsamples to around 4,000,000 for the 100 cm × 100 cm samples.

3. Result and discussion

3.1. Geometrical measurement results

The physical apertures and their standard deviations of the fractures under varying normal stresses are presented in Table 2, along with the average displacement recorded by the LVDTs. The difference between the LVDT measurements and the photogrammetric method for determining aperture closure during the application of normal stresses is negligible, with a deviation of approximately 1–8 μm. This indicates that photogrammetry can detect changes in the fracture dimensions that closely align with LVDT readings. Consequently, it enhances the simulation of physical aperture under normal stress because physical aperture changes do not occur uniformly across the surface. Due to the distribution of physical apertures and their asperities, some areas may come into contact more than others. While LVDTs can accurately measure changes in their positions, translating these movements into numerical modeling can be challenging. Often, the average displacement recorded by the LVDTs is used, assuming uniform movement across the sample, which may not accurately reflect the behavior of the fracture. This averaging process can lead to approximations, particularly when only a portion of the fracture surface moves in response to the applied stress.

Fig. 6 illustrates the photogrammetric aperture field and contact areas of Sample 3. As normal stresses increased, the green areas

representing open apertures gradually changed to blue, indicating closure, as shown in Fig. 6a through 6d. The contact areas also increased by applying higher normal stresses across these figures. Additionally, Fig. 7a and b display the aperture fields of samples 1 and 2 under zero normal stress, respectively.

Fig. 8 shows the mean roughness (\bar{Z}_2) and JRC values, along with their standard deviations, for three samples. These values were calculated using Eqs. (1)–(4) for both the X and Y directions. As shown in Fig. 8, the calculated roughness and JRC values in the Y direction are higher than those in the X direction for samples 1 and 2. For Sample 3, the values are nearly identical, although the X direction is slightly rougher than the Y direction. This observation indicates roughness anisotropy.

3.2. Experimental results

Fig. 9 illustrates the experimental results relating to flow rate to pressure gradient under different normal stress conditions. The nonlinear trend indicates that the Forchheimer equation is applicable for analyzing the data. Using the outcomes of the regression analysis, the Forchheimer coefficients (A and B) were determined using Eq. (12). The hydraulic aperture (e_h) was calculated with Eq. (14), while β was computed using Eq. (15). These results are summarized in Table 3, with R-squared values for all fittings exceeding 99 %.

As normal stresses increase, the Forchheimer coefficients A and B, as well as the non-Darcy coefficient β , show an upward trend (Fig. 10). This increase is primarily due to the decrease in physical aperture, which restricts potential fluid pathways and enhances contact areas. As a result, this leads to increased tortuosity and nonlinearity in fluid flow, intensified by elevated inertial effects (Eq. (15)). When normal stress increased and physical aperture is reduced, both the linear coefficient (A) and the nonlinear coefficients (B and β) increased.

Further analysis reveals anisotropy in the Forchheimer coefficients and the non-Darcy coefficient, as they vary with direction. For instance, the linear coefficient A is smaller in the X direction for samples 1 and 2 compared to the Y direction (Fig. 10a). Correspondingly, roughness values in the X direction for these samples are also lower than in the Y direction (Fig. 8). In Sample 3, the nonlinear coefficient B is higher in the X direction due to relatively high roughness (Fig. 10b). The non-Darcy coefficient β shows a similar relationship with roughness, except in Sample 3, where the roughness values are nearly identical (Fig. 10c). This comparison indicates that fractures with higher roughness correspond to larger A and B values, suggesting that increased roughness results in greater tortuosity in fluid flow and reduced conductivity (Fig. 10).

The linear coefficient (A) and the non-linear coefficient (B) are influenced by the roughness and irregular physical aperture of a

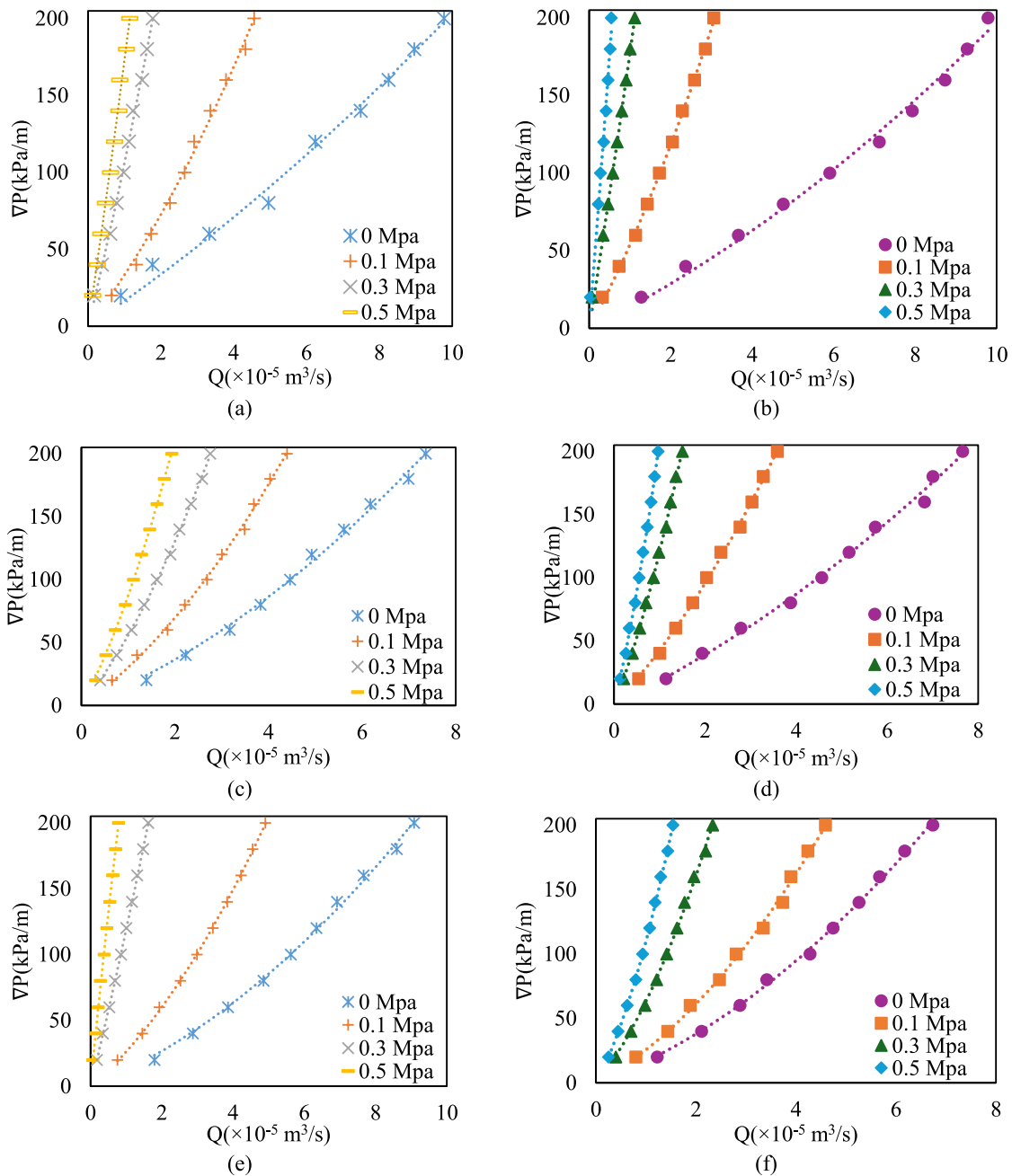


Fig. 9. The relationship between the pressure gradient and the flow rate of rough fractures under different normal stresses for two perpendicular directions, X (a, c, e) and Y (b, d, f).

fracture. The linear coefficient (A) is significantly influenced by roughness and irregularities in the physical aperture of a fracture, which directly affect viscous losses. Rough surfaces increase friction between the fluid and the fracture walls, particularly near sharp edges and contact points. Rapid changes in flow velocity in these regions further intensify friction, resulting in greater viscous energy loss.

In narrow physical apertures, fluid movement near the walls slows down, resulting in increased viscous energy dissipation. Additionally, the increase in normal stress and the resulting presence of more tiny physical apertures contribute to greater energy losses. This combination of factors results in a higher linear coefficient (A) (Fig. 10a) and a reduction in hydraulic aperture (Fig. 11), especially in fractures with rougher surfaces and smaller physical apertures.

The nonlinear coefficient (B) is associated with inertial losses. As

fluid flows through a rough fracture with an irregular physical aperture, it must continuously adjust its speed when transitioning between narrower and wider sections. Sharp edges and rough surfaces create eddies due to changes in the fluid’s momentum, leading to additional inertial energy losses. These eddy flows increase the nonlinearity observed in flow behavior and raise the nonlinear coefficient (B). Furthermore, the conditions of increased normal stress and the presence of numerous tiny regions result in longer, more tortuous paths for the fluid, contributing to greater inertial losses (Fig. 10b and c). Thus, the nonlinear coefficient (B) tends to increase with rougher surfaces and smaller apertures.

To assess the anisotropic behavior of fluid flow in rough fractures, a comparison was made between the hydraulic apertures obtained in two perpendicular directions, X and Y, as illustrated in Fig. 11. The results indicate that even a small increase in normal stress leads to a significant

Table 3
The parametric analysis data obtained by regression according to Forchheimer equation in two perpendicular directions.

Sample number	Normal stress (MPa)	Direction							
		X				Y			
		$A_X (\times 10^9 \text{ kg/sm}^5)$	$B_X (\times 10^{12} \text{ kg/m}^8)$	$e_{hX} (\mu\text{m})$	$\beta_X (\text{m}^{-1})$	$A_Y (\times 10^9 \text{ kg/sm}^5)$	$B_Y (\times 10^{12} \text{ kg/m}^8)$	$e_{hY} (\mu\text{m})$	$\beta_Y (\text{m}^{-1})$
1	0	1.6	4.35	299	24.29	1.31	6.66	320	42.49
	0.1	3.04	29.4	241	107	4.84	53.5	207	142.81
	0.3	9.76	85	164	142.15	16.9	86.8	136	100.67
	0.5	16.1	118	138	141.35	33.9	254	108	185.21
2	0	1.49	16.8	306	98.65	1.73	11.1	291	59.01
	0.1	2.57	45.6	255	185.41	3.74	51.8	225	164.4
	0.3	4.64	93.9	210	258.04	9.13	290	167	506.64
	0.5	6.91	183	184	386	14.80	600	142	760.51
3	0	1.47	19.9	307	118	1.42	23.6	311	142.68
	0.1	2.27	36.6	266	161.8	2.06	49.8	275	234.99
	0.3	11.2	70.7	156	107.96	4.62	171	210	470.73
	0.5	20	300	129	310.98	7.18	380	181	781.11

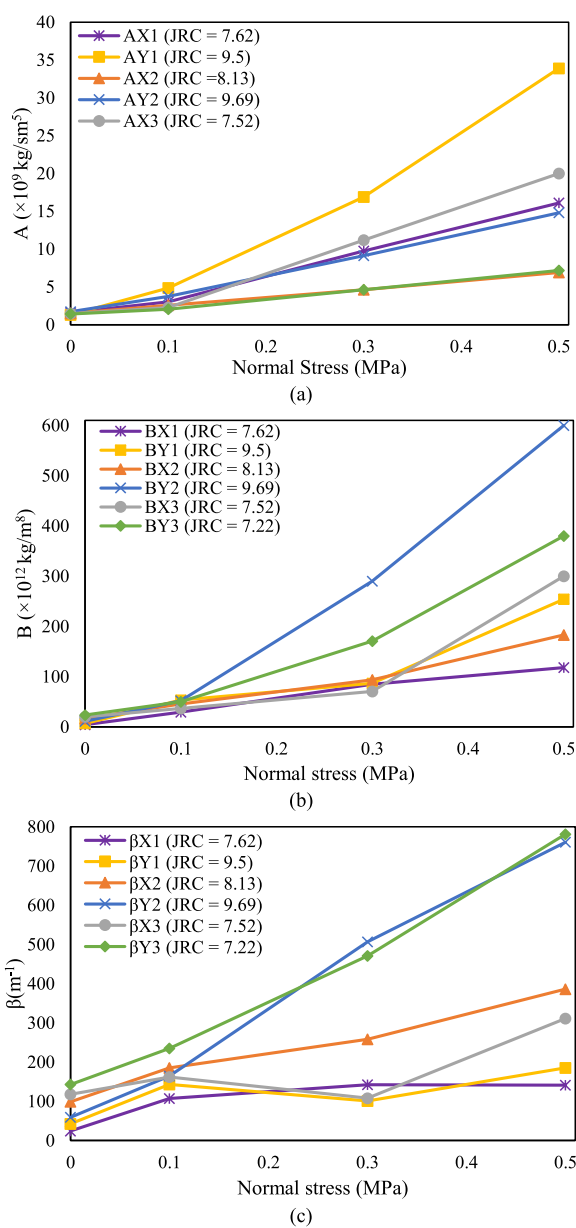


Fig. 10. Comparison between Forchheimer coefficients A (a) and B (b), and non-Darcy coefficient β (c) in perpendicular directions under varying normal stresses for Sample 1, Sample 2, and Sample 3.

decrease in hydraulic apertures (Fig. 11). Anisotropy was observed in all samples, with Samples 1 and 2 exhibiting higher hydraulic apertures in the X direction alongside lower JRC values, which suggests greater conductivity along this axis compared to the Y direction, which has higher roughness values (Fig. 11a and b). Conversely, for Sample 3, the Y direction displayed higher conductivity with lower roughness than the X direction, which had greater roughness (Fig. 11c).

The Forchheimer coefficients (A and B) are influenced by the directional roughness, reflecting the anisotropic nature of the fracture surfaces. Anisotropic analysis of Samples 1 to 3 under varying normal stresses reveals that directions with higher roughness values typically correspond to higher A and B coefficients. Additionally, as normal stresses increase, these coefficients tend to rise. Increased contact points can induce turbulence and nonlinearity in fluid flow through the fracture in directions with higher roughness, resulting in lower hydraulic apertures (see Fig. 11).

3.3. Results of numerical flow simulation

Fluid flow through single fractures was validated by comparing the experimental results with real 3D models reconstructed in COMSOL using photogrammetric 3D point clouds, as described in Section 2.5. As part of the comparison study, Fig. 12 shows experimental and numerical data under normal stresses of 0, 0.1, 0.3, and 0.5 MPa for Sample 2 in the X direction at a pressure gradient of 40 kPa/m (Fig. 12a), and for Sample 3 in the Y direction at a pressure gradient of 120 kPa/m (Fig. 12b). The comparison demonstrates that the numerical modeling and photogrammetric 3D model can obtain results similar to those observed in the laboratory. Additionally, Fig. 12c shows Sample 1 under normal stress of 0.1 MPa in the X direction, where the numerical results closely followed the nonlinearity observed in the experimental data. The calculated hydraulic aperture from the numerical results was 255 μm , compared to 241 μm from the experimental data. For the β , the numerical result was 123.45 m^{-1} , while the experimental value was 107 m^{-1} . The numerical and experimental results are closely aligned, demonstrating that numerical modeling using 3D photogrammetric models is effective for simulating fluid flow through a fracture.

Fig. 13 shows simulations of Sample 2 with a pressure gradient of 60 kPa/m under normal stresses of 0 and 0.5 MPa in the X direction. The physical aperture is 478 μm at zero normal stress, decreasing to 451 μm under normal stress of 0.5 MPa. In Fig. 13a, nearly parallel streamlines can be observed along the fracture without normal stress. In contrast, Fig. 13b illustrates more channelized flow with increased tortuosity under 0.5 MPa. A comparison of the streamlines under different normal stresses reveals that higher stresses lead to tortuous flow channels with longer streamlines. This occurs as contact areas (depicted in blue) increase with applied normal stress, causing greater frictional resistance across the rough fracture surfaces. These factors together contribute to

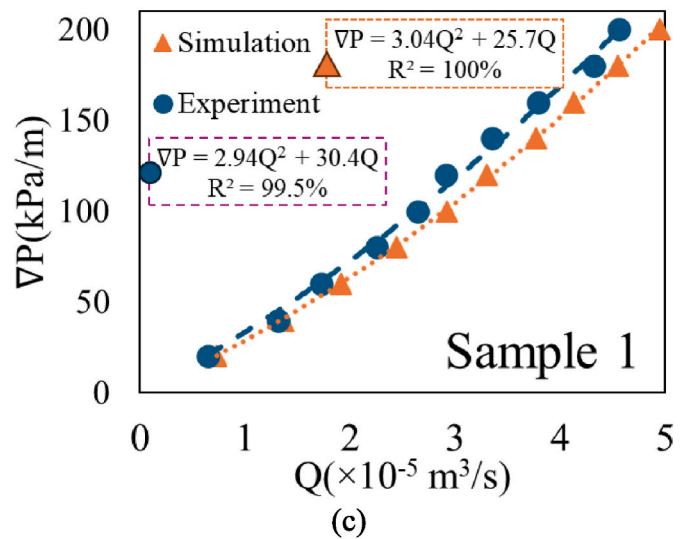
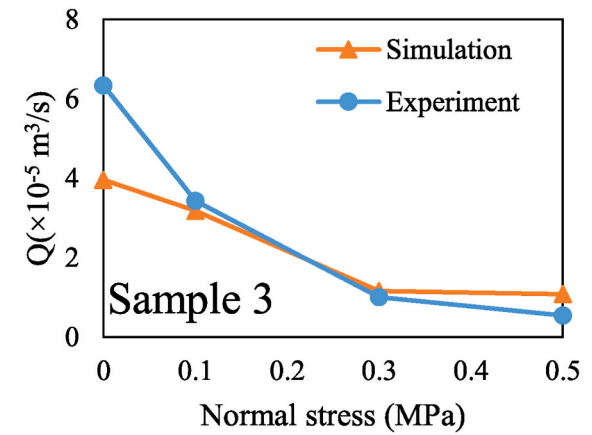
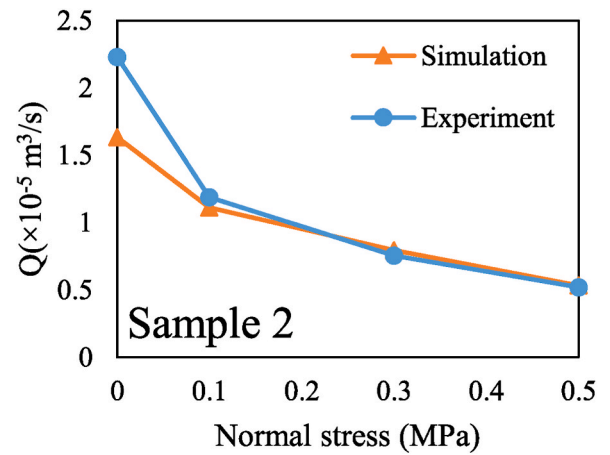
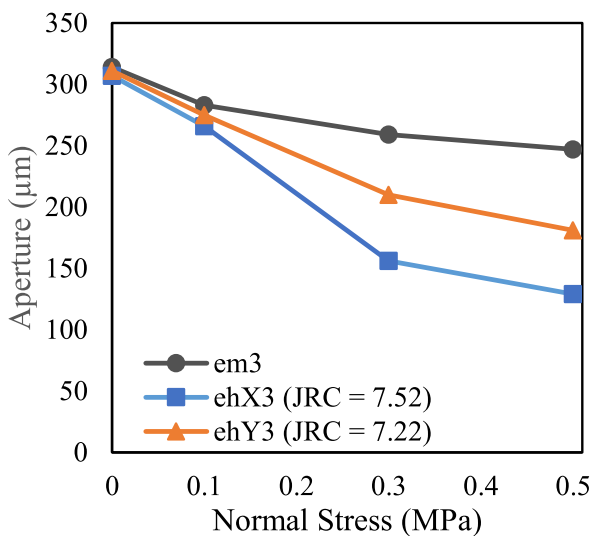
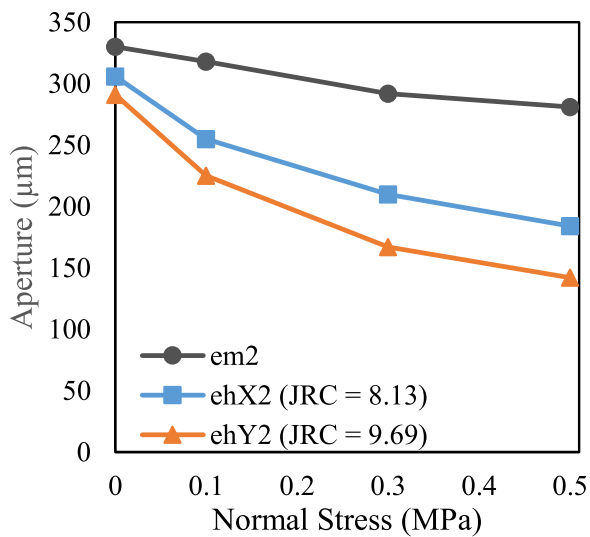
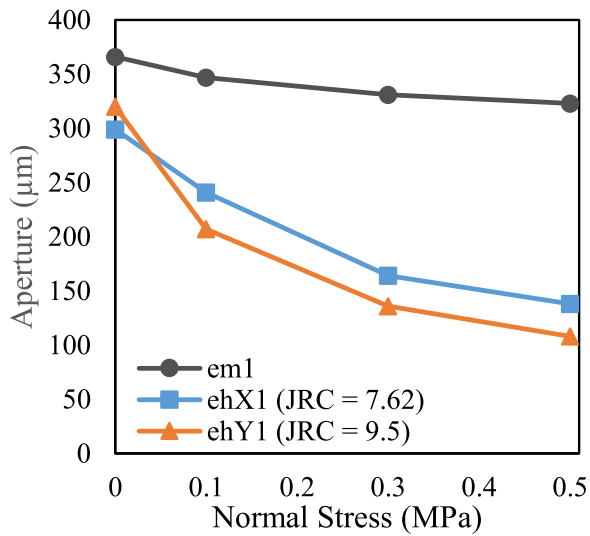


Fig. 11. Comparison between hydraulic apertures in perpendicular directions under varying normal stresses, (a) Sample 1, (b) Sample 2, and (c) Sample 3.

Fig. 12. Comparison of experimental and simulated flow rates for different pressure gradients under various normal stresses: (a) Sample 2 in the X direction at a pressure gradient of 40 kPa/m, (b) Sample 3 in the Y direction at a pressure gradient of 120 kPa/m, and (c) comparison between experimental and numerical results for Sample 1 under normal stress of 0.1 MPa.

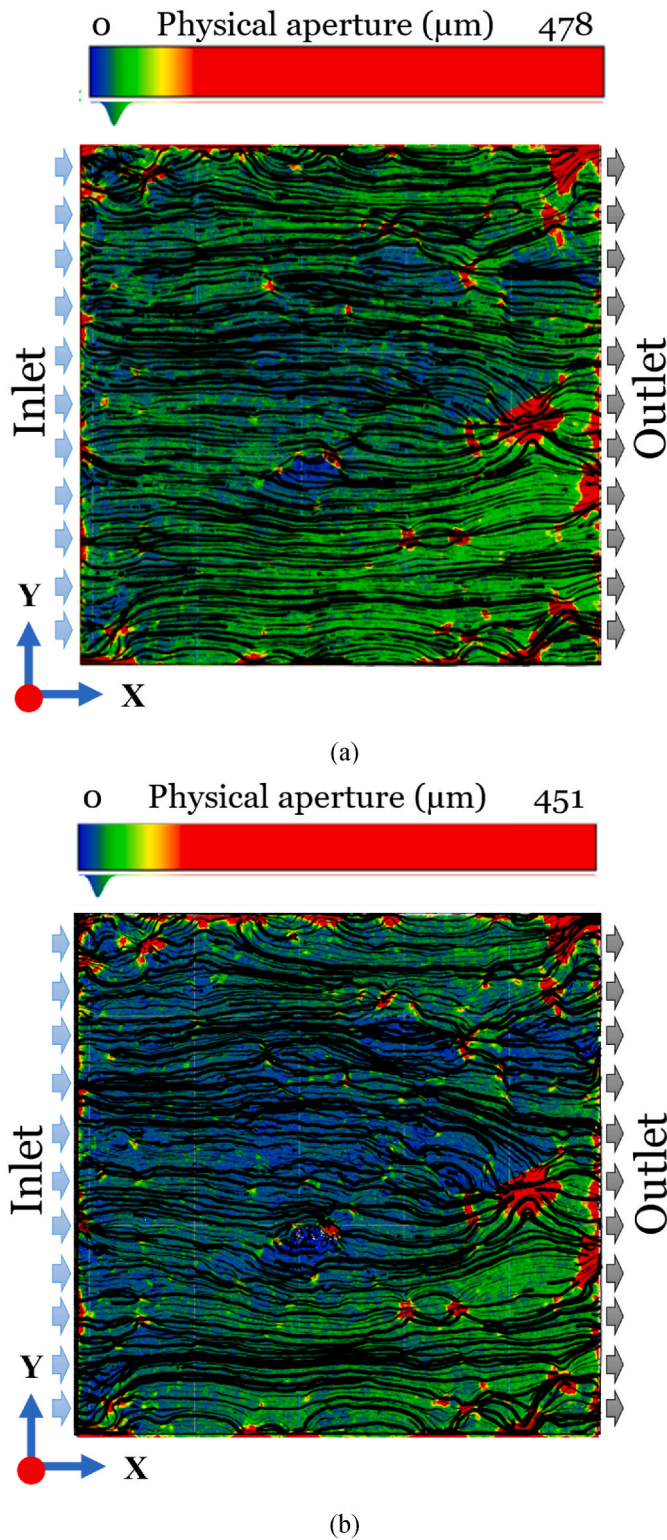


Fig. 13. Streamlines through Sample 2 under different normal stresses (a) 0 MPa, and (b) 0.5 MPa, at a pressure gradient of 60 kPa/m in the direction X. The histograms show the physical aperture distribution of the fracture.

the reduction in flow rates.

3.4. Scale effect results

If numerical modeling results of fluid flow simulation were verified with experimental results, the numerical modeling can be adopted to

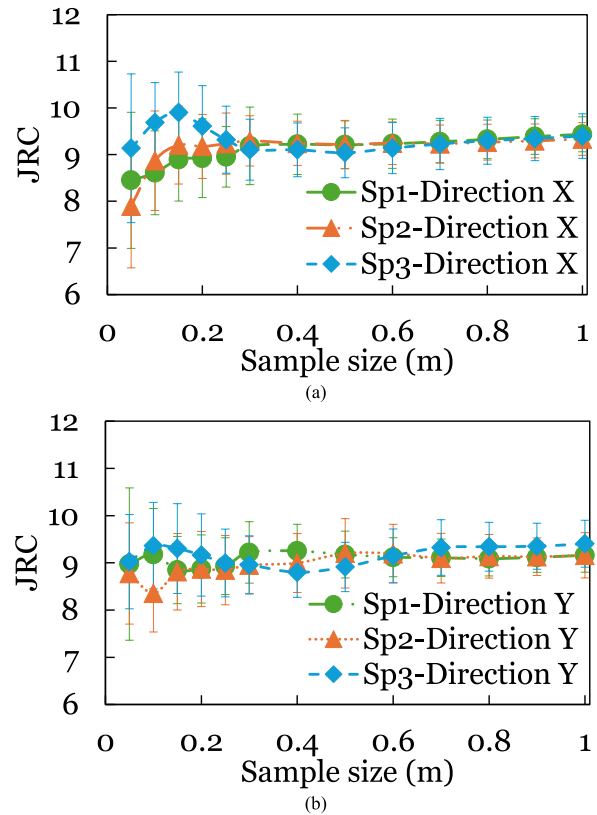


Fig. 14. The relationship between JRC values and sample sizes for subsamples extracted from Sp1, Sp2, and Sp3 is shown for two perpendicular directions: X (a) and Y (b). The confidence interval, calculated as the standard deviation, is represented by the error bars. The results for Sp1 have been modified after.⁷⁵

study the scale effect on fracture permeability in samples Sp1, Sp2, and Sp3. Fig. 14 illustrates the mean JRC values along with their standard deviations for subsamples extracted from Sp1, Sp2, and Sp3 samples with lengths ranging from 5 cm to 100 cm. The mean JRC values exhibit a stable trend from sample side lengths of 30 cm onwards, where the deviation of mean JRC becomes insignificant. Simultaneously, the standard deviation experiences a decreasing trend. This reduction in variation can be attributed to the increase in the overlapped length of larger profiles (Fig. 5). The JRC is approximately 9 for samples Sp1, Sp2, and Sp3. Also, there are no significant differences between directions X (Fig. 14a) and Y (Fig. 14b).

The outcomes of numerical simulations for samples Sp1, Sp2, and Sp3 are depicted in Fig. 15, considering various sample sizes in both the X and Y directions. By applying regression and fitting Eq. (12) to the data, the Forchheimer coefficients (A and B) were calculated (Fig. 16). As the sample size increased, the Forchheimer coefficients exhibited a decreasing trend, indicating a negative scale effect. This negative trend for linear coefficient A and nonlinear coefficient B can be attributed to several factors, including roughness and aperture. In this study, the physical aperture was assumed constant, leaving roughness as a key factor influencing the coefficients as sample sizes increased.

For sample sizes below 30 cm, roughness varied significantly, with some regions showing higher local roughness than others. The viscous losses, represented by coefficient A, were higher in these rough regions due to increased friction. Fig. 16a and c show a steep change in coefficient A for sample sizes under 30 cm, after which surface roughness variation stabilizes (see Fig. 14). With roughness no longer changing significantly, the fluid path remained relatively constant. Consequently, viscous losses, rooted in friction between the surface and the flow, decrease, resulting in a negative trend with increasing sample size. A

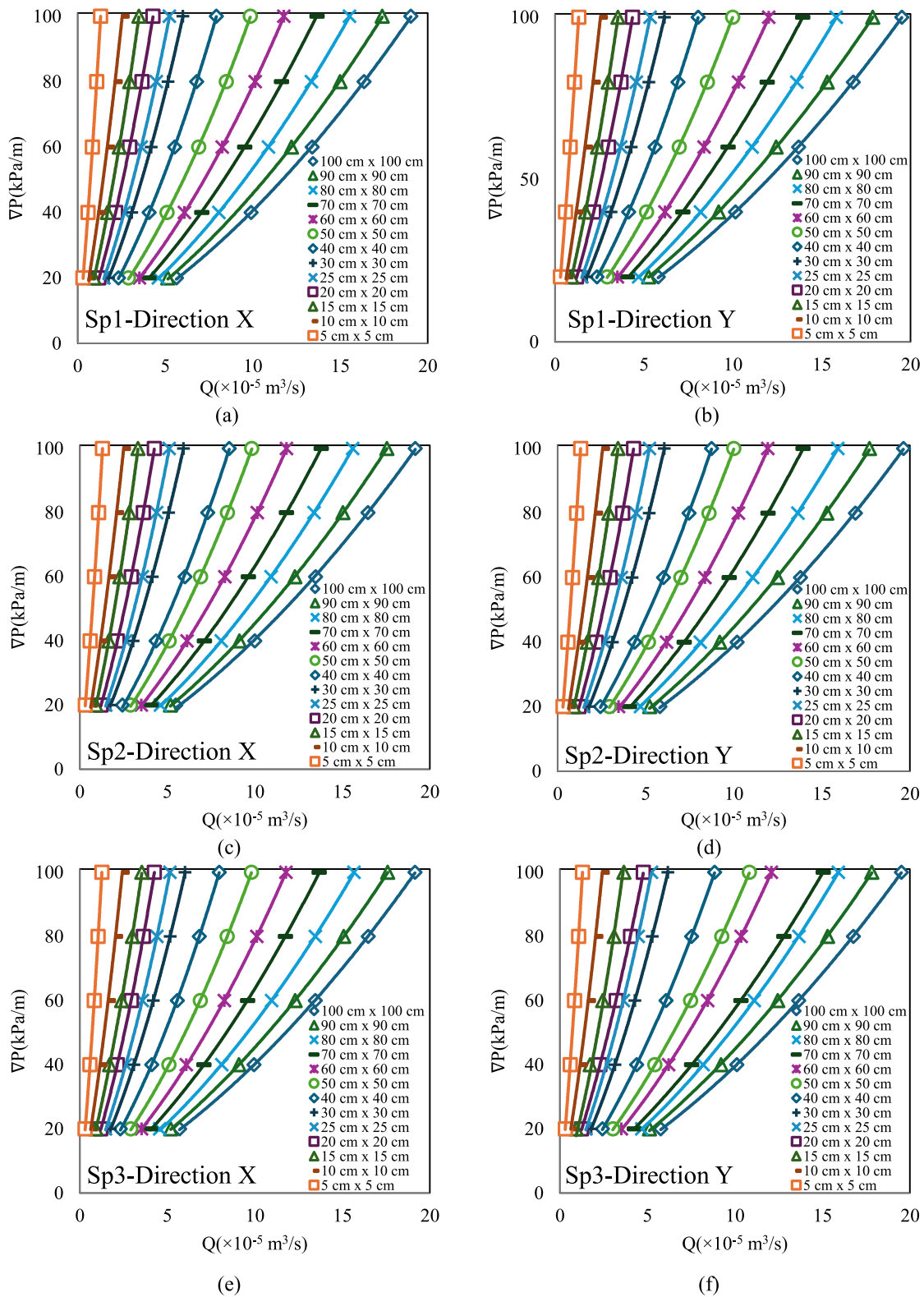


Fig. 15. The relationship between the pressure gradient and the flow rate of rough fractures for different sample sizes extracted from samples Sp1, Sp2, and Sp3 for two perpendicular directions, X (a, c, e) and Y (b, d, f). (Fig. 15 a and b modified after ⁷⁵).

surface with consistent roughness (negligible changes after 30 cm) appears to lead to less viscous energy loss, causing the slope in Fig. 16a and b to change more gradually. This finding is also reflected in the calculated hydraulic aperture (Fig. 17a and c), which shows stability after 30 cm.

The same reasoning applies to the non-linear coefficient B, associated with inertial losses. As the fracture's geometrical properties, such as roughness (Fig. 14), stabilize with larger sample sizes, the fluid flow becomes more consistent, with fewer disruptions and lower inertial losses. Fig. 16b and d show that coefficient B experiences steep changes

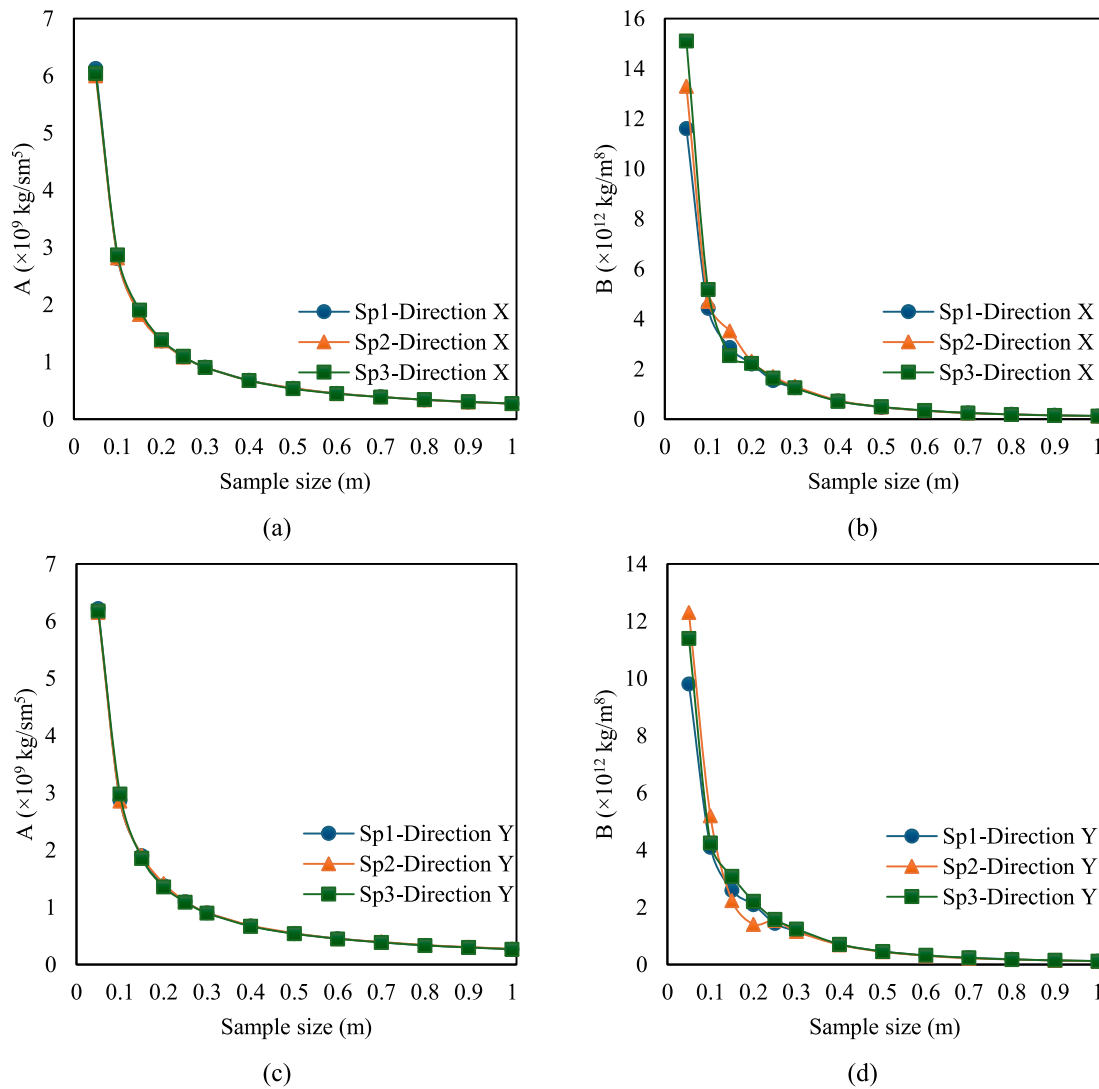


Fig. 16. The calculated Forchheimer coefficients (A and B) versus sample sizes extracted from samples Sp1, Sp2, and Sp3 for two perpendicular directions, X (a and b) and Y (c and d).

for sample sizes under 30 cm but becomes more stable afterward. The flow becomes more uniform, minimizing significant changes that could affect turbulence and lead to inertial losses in larger samples. Additionally, Fig. 17b and d illustrate that the non-Darcy coefficient for different sample sizes indicates that after 30 cm, turbulence and non-uniformity in fluid flow diminish.

Hydraulic aperture and non-Darcy coefficients, calculated according to Eqs. (14) and (15) for different sample sizes, are illustrated in Fig. 17. Significant variability is observed in hydraulic aperture and non-Darcy coefficients for sample sizes smaller than 30 cm. However, beyond this threshold, the hydraulic aperture stabilizes at approximately 340 μm , and the non-Darcy coefficient stabilizes at around 140 m^{-1} , with minimal changes. This specific sample size, around 30 cm, can be interpreted as the representative size for hydraulic aperture, non-Darcy coefficients, and JRC values, providing a stable and meaningful reference point in the analysis.

4. Conclusion

Fluid flow tests were conducted on three Kuru grey granite tensile fractures, each measuring 25 cm \times 25 cm \times 10 cm, under different normal stresses. High-precision photogrammetry was used to

reconstruct 3D models of the fractures and measure the physical aperture at each normal stress state. The nonlinear experimental results were accurately modeled using the Forchheimer equation. These photogrammetric models were then utilized to simulate fluid flow numerically. The Navier-Stokes equations were applied, and the numerical results aligned with the experimental tests, also following the Forchheimer equation. A numerical study on scale effects was carried out for various subsample sizes extracted from 1 m \times 1 m samples, derived from a 3D rough surface measuring 2 m \times 1 m.

The key conclusions drawn from this study are as follows.

1. The photogrammetric method was used to reconstruct high-precision 3D models of the fractures. These 3D models were constructed in COMSOL using the obtained 3D point clouds, and the numerical results closely matched the real water flow test results, showing minimal deviations in flow rate.
2. Increasing normal stress led to an increase in the Forchheimer coefficients, attributed to a reduction in potential flow paths and an increase in flow complexity. Higher normal stress induces more nonlinear flow patterns, influencing the observed rise in the Forchheimer coefficients.

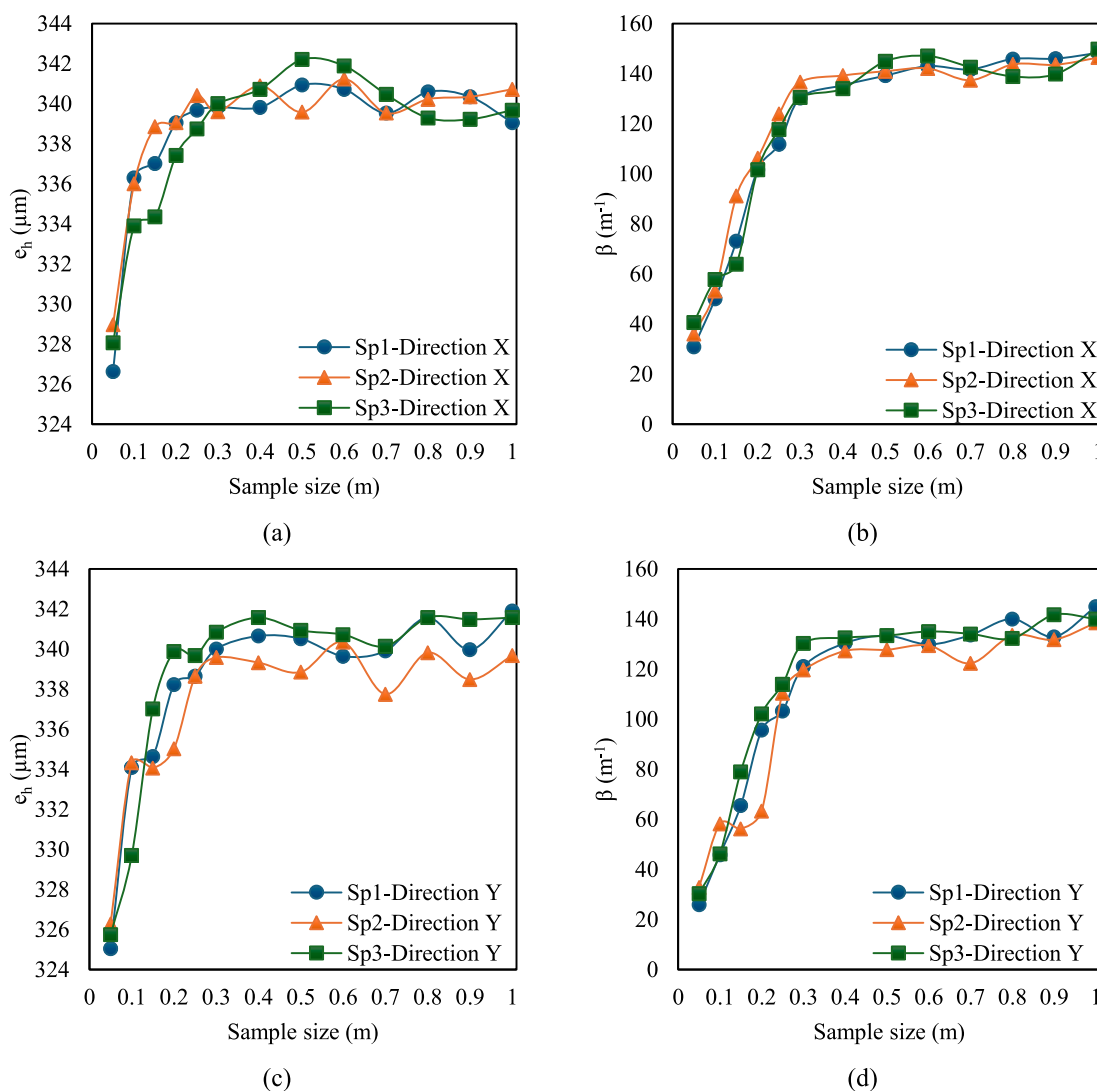


Fig. 17. The calculated hydraulic aperture (e_h) and non-Darcy coefficient (β) versus sample sizes extracted from samples Sp1, Sp2, and Sp3 for two perpendicular directions, X (a and b) and Y (c and d).

- Anisotropy was evident when roughness values were measured in different directions. Forchheimer coefficients were influenced by roughness, with higher roughness values corresponding to higher coefficients.
- For the $1 \text{ m} \times 1 \text{ m}$ samples extracted from the $2 \text{ m} \times 1 \text{ m}$ 3D rough surface of Kuru grey granite, the representative sample size for roughness, hydraulic aperture, and non-Darcy coefficient stabilization was found to be $30 \text{ cm} \times 30 \text{ cm}$. Beyond this size, values stabilized, with a JRC of around 9, hydraulic aperture at approximately $340 \mu\text{m}$, and a non-Darcy coefficient of around 140 m^{-1} . The Forchheimer coefficients exhibited a negative trend with increasing sample size, indicating a strong scale effect on both linear and nonlinear coefficients.

CRediT authorship contribution statement

Masoud Torkan: Writing – original draft, Visualization, Validation, Software, Methodology, Formal analysis, Data curation, Conceptualization, Funding acquisition. **Lauri Uotinen:** Writing – review & editing, Project administration, Funding acquisition. **Alireza Baghbanan:** Writing – review & editing, Conceptualization. **Mikael Rinne:** Writing – review & editing, Supervision, Project administration.

Statements and declarations

Part of the source data was used in a conference paper submitted to EUROCK 2024.⁷⁵

Declaration of generative AI and AI-assisted technologies in the writing process

During the preparation of this work the authors used ChatGPT in order to check the language and improve the readability. After using ChatGPT, the authors reviewed and edited the content as needed and take full responsibility for the content of the publication.

Funding

This work was made possible thanks to the funding provided by the State Nuclear Waste Management Fund (VYR) and the support of the Ministry of Economic Affairs and Employment of Finland on the Finnish Research Programme on Nuclear Waste Management KYT2018 and KYT2022 of the Nuclear Energy Act (990/1987) in the research projects Fluid flow in fractured hard rock mass (RAKKA), funding numbers KYT January 2021 and KYT January 2022. Additional support was received

from the National Nuclear Safety and Waste Management Research Programme SAFER2028, funding numbers SAFER 25/2023 (MIRKA) and SAFER 42/2023 (CORF).

Declaration of competing interest

The authors declare the following financial interests/personal relationships which may be considered as potential competing interests: Mikael Rinne reports financial support was provided by Ministry of Economic Affairs and Employment of Finland. If there are other authors, they declare that they have no known competing financial interests or personal relationships that could have appeared to influence the work reported in this paper.

The research was carried out without the involvement of the funding sources, and there is no conflict of interest.

Data availability

Data will be made available on request.

References

- Singhal BBS, Gupta RP. *Applied Hydrogeology of Fractured Rocks*. second ed. ed. Springer Dordrecht; 2010. <https://doi.org/10.1007/978-90-481-8799-7>.
- Zimmerman RW, Bodvarsson GS. Hydraulic conductivity of rock fractures. *Transp Porous Media*. 1996;23(1):1–30. <https://doi.org/10.1007/BF00145263>.
- Baghbanan A, Jing L. Stress effects on permeability in a fractured rock mass with correlated fracture length and aperture. *Int J Rock Mech Min Sci*. 2008;45(8):1320–1334. <https://doi.org/10.1016/j.ijrmms.2008.01.015>.
- Singh KK, Singh DN, Ranjith PG. Laboratory simulation of flow through single fractured granite. *Rock Mech Rock Eng*. 2015;48(3):987–1000. <https://doi.org/10.1007/s00603-014-0630-9>.
- Hakami E, Larsson E. Aperture measurements and flow experiments on a single natural fracture. *Int J Rock Mech Min Sci Geomech Abstr*. 1996;33(4):395–404. [https://doi.org/10.1016/0148-9062\(95\)00070-4](https://doi.org/10.1016/0148-9062(95)00070-4).
- Singh KK, Singh DN, Ranjith PG. Simulating flow through fractures in a rock mass using analog material. *Int J GeoMech*. 2014;14(1):8–19. [https://doi.org/10.1061/\(ASCE\)GM.1943-5622.0000295](https://doi.org/10.1061/(ASCE)GM.1943-5622.0000295).
- You B, Xu J, Shi S, Liu H, Lu Y, Li H. Effect of stress and water pressure on permeability of fractured Sandstone based on response surface method. *Front Earth Sci*. 2020;8. <https://doi.org/10.3389/feart.2020.00011>.
- Shahbazi A, Saeidi A, Chesnaux R. A review of existing methods used to evaluate the hydraulic conductivity of a fractured rock mass. *Eng Geol*. 2020;265, 105438. <https://doi.org/10.1016/j.enggeo.2019.105438>.
- Zhang Y, Chai J. Effect of surface morphology on fluid flow in rough fractures: a review. *J Nat Gas Sci Eng*. 2020;79, 103343. <https://doi.org/10.1016/j.jngse.2020.103343>.
- Corradetti A, McCaffrey K, De Paola N, Tavani S. Evaluating roughness scaling properties of natural active fault surfaces by means of multi-view photogrammetry. *Tectonophysics*. 2017;717:599–606. <https://doi.org/10.1016/j.tecto.2017.08.023>.
- Zambrano M, Pitts AD, Salama A, Volatili T, Giorgioni M, Tondi E. Analysis of fracture roughness control on permeability using SfM and fluid flow simulations: implications for carbonate reservoir characterization. *Geofluids*. 2019;2019, 4132386. <https://doi.org/10.1155/2019/4132386>.
- Keller A. High resolution, non-destructive measurement and characterization of fracture apertures. *Int J Rock Mech Min Sci*. 1998;35(8):1037–1050. [https://doi.org/10.1016/S0148-9062\(98\)00164-8](https://doi.org/10.1016/S0148-9062(98)00164-8).
- Tatone BSA, Grasselli G. Quantitative measurements of fracture aperture and directional roughness from rock cores. *Rock Mech Rock Eng*. 2012;45(4):619–629. <https://doi.org/10.1007/s00603-011-0219-5>.
- Torkan M, Janiszewski M, Uotinen L, Baghbanan A, Rinne M. Photogrammetric method to determine physical aperture and roughness of a rock fracture. *Sensors*. 2022;22(11):4165. <https://doi.org/10.3390/s22114165>.
- Gentier SS, Hopkins DL. Mapping fracture aperture as a function of normal stress using a combination of casting, image analysis and modeling techniques. *Int J Rock Mech Min Sci*. 1997;34(3). [https://doi.org/10.1016/S1365-1609\(97\)00234-7](https://doi.org/10.1016/S1365-1609(97)00234-7), 132.e131–132.e114.
- Louis CA. Study of groundwater flow in jointed rock and its influence on the stability of rock masses. *Imperial College Rock Mech Res*. 1969;(10):1–90.
- Koyama T, Fardin N, Jing L, Stephansson O. Numerical simulation of shear-induced flow anisotropy and scale-dependent aperture and transmissivity evolution of rock fracture replicas. *Int J Rock Mech Min Sci*. 2006;43(1):89–106. <https://doi.org/10.1016/j.ijrmms.2005.04.006>.
- Kilbury RK, Rasmussen TC, Evans DD, Warrick AW. Water and air intake of surface-exposed rock fractures in situ. *Water Resour Res*. 1986;22(10):1431–1443. <https://doi.org/10.1029/WR022i010p1431>.
- Tsang YW. Usage of “Equivalent apertures” for rock fractures as derived from hydraulic and tracer tests. *Water Resour Res*. 1992;28(5):1451–1455. <https://doi.org/10.1029/92WR00361>.
- Barton N, Choubey V. The shear strength of rock joints in theory and practice. *Rock Mech*. 1977;10(1):1–54. <https://doi.org/10.1007/BF01261801>.
- Raven KG, Gale JE. Water flow in a natural rock fracture as a function of stress and sample size. *Int J Rock Mech Min Sci Geomech Abstr*. 1985;22(4):251–261. [https://doi.org/10.1016/0148-9062\(85\)92952-3](https://doi.org/10.1016/0148-9062(85)92952-3).
- Qian J, Zhan H, Zhao W, Sun F. Experimental study of turbulent unconfined groundwater flow in a single fracture. *J Hydrol*. 2005;311(1):134–142. <https://doi.org/10.1016/j.jhydrol.2005.01.013>.
- Zhang Q, Luo S, Ma H, Wang X, Qian J. Simulation on the water flow affected by the shape and density of roughness elements in a single rough fracture. *J Hydrol*. 2019; 573:456–468. <https://doi.org/10.1016/j.jhydrol.2019.03.069>.
- Whitaker S. The Forchheimer equation: a theoretical development. *Transp Porous Media*. 1996;25(1):27–61. <https://doi.org/10.1007/BF00141261>.
- Kohl T, Evans KF, Hopkirk RJ, Jung R, Rybach L. Observation and simulation of non-Darcian flow transients in fractured rock. *Water Resour Res*. 1997;33(3):407–418. <https://doi.org/10.1029/96WR03495>.
- Elsworth D, Goodman RE. Characterization of rock fissure hydraulic conductivity using idealized wall roughness profiles. *Int J Rock Mech Min Sci Geomech Abstr*. 1986; 23(3):233–243. [https://doi.org/10.1016/0148-9062\(86\)90969-1](https://doi.org/10.1016/0148-9062(86)90969-1).
- Scesi L, Gattinoni P. Roughness control on hydraulic conductivity in fractured rocks. *Hydrogeol J*. 2007;15(2):201–211. <https://doi.org/10.1007/s10040-006-0076-6>.
- Ma C, Chen Y, Tong X, Ma G. An equivalent analysis of non-linear flow along rough-walled fractures based on power spectrum and wavelet transform. *J Hydrol*. 2023; 620, 129351. <https://doi.org/10.1016/j.jhydrol.2023.129351>.
- Li B, Jiang Y, Koyama T, Jing L, Tanabashi Y. Experimental study of the hydro-mechanical behavior of rock joints using a parallel-plate model containing contact areas and artificial fractures. *Int J Rock Mech Min Sci*. 2008;45(3):362–375. <https://doi.org/10.1016/j.ijrmms.2007.06.004>.
- Chen Y, Liang W, Lian H, Yang J, Nguyen VP. Experimental study on the effect of fracture geometric characteristics on the permeability in deformable rough-walled fractures. *Int J Rock Mech Min Sci*. 2017;98:121–140. <https://doi.org/10.1016/j.ijrmms.2017.07.003>.
- Wei X, Ma H, Qian J, Ma L. Study on the geometric characteristics effect of contact area on fracture seepage. *Phys Fluids*. 2023;35(1). <https://doi.org/10.1063/5.0131145>.
- Kulatilake PHSW, Park J, Su X-p. Fluid flow through natural single-rock fractures: experimental and numerical investigations. *Int J GeoMech*. 2020;20(10), 04020168. [https://doi.org/10.1061/\(ASCE\)GM.1943-5622.0001790](https://doi.org/10.1061/(ASCE)GM.1943-5622.0001790).
- Witherspoon PA, Wang JSY, Iwai K, Gale JE. Validity of Cubic Law for fluid flow in a deformable rock fracture. *Water Resour Res*. 1980;16(6):1016–1024. <https://doi.org/10.1029/WR016i006p1016>.
- Forchheimer P. Wasserbewegung durch boden. *Z Des Vereines Dtsch Ingenieure*. 1901; 45(50):1781–1788.
- Izbash SV. *O Filtracii V Kropnozernstom Materiale*. Nauchnoissled, Inst Hidrotechniki (NIIG). 1931.
- Zoorabadi M, Saydam S, Timms W, Hebblewhite B. Non-linear flow behaviour of rough fractures having standard JRC profiles. *Int J Rock Mech Min Sci*. 2015;76: 192–199. <https://doi.org/10.1016/j.ijrmms.2015.03.004>.
- Wang Z, Liu J, Zheng T, Qiao L, Li K. Macroscopic and mesoscopic characteristics of radial flow in rough rock fractures. *Rock Mech Rock Eng*. 2023. <https://doi.org/10.1007/s00603-023-03312-4>.
- Chen Y-F, Zhou J-Q, Hu S-H, Hu R, Zhou C-B. Evaluation of Forchheimer equation coefficients for non-Darcy flow in deformable rough-walled fractures. *J Hydrol*. 2015;529:993–1006. <https://doi.org/10.1016/j.jhydrol.2015.09.021>.
- Rong G, Hou D, Yang J, Cheng L, Zhou C. Experimental study of flow characteristics in non-mated rock fractures considering 3D definition of fracture surfaces. *Eng Geol*. 2017;220:152–163. <https://doi.org/10.1016/j.enggeo.2017.02.005>.
- Li M, Liu X, Li Y, Hou Z, Qiao S. Effect of contact areas on seepage behavior in rough fractures under normal stress. *Int J GeoMech*. 2022;22(4), 04022019. [https://doi.org/10.1061/\(ASCE\)GM.1943-5622.0002330](https://doi.org/10.1061/(ASCE)GM.1943-5622.0002330).
- Yin P, Zhao C, Ma J, Yan C, Huang L. Experimental study of non-linear fluid flow through rough fracture based on fractal theory and 3D printing technique. *Int J Rock Mech Min Sci*. 2020;129, 104293. <https://doi.org/10.1016/j.ijrmms.2020.104293>.
- Luo Y, Zhang Z, Zhang L, Xue K, Long K. Influence of fracture roughness and void space morphology on nonlinear fluid flow through rock fractures. *Eur Phys J Plus*. 2022;137(11):1288. <https://doi.org/10.1140/epjp/s13360-022-03499-5>.
- Chen Y, Selvadurai APS, Zhao Z. Modeling of flow characteristics in 3D rough rock fracture with geometry changes under confining stresses. *Comput Geotech*. 2021;130, 103910. <https://doi.org/10.1016/j.compgeo.2020.103910>.
- Yang H, Wang X, Yu L, Liu R. Effects of contact area and contact shape on nonlinear fluid flow properties of fractures by solving Navier-Stokes equations. *Lithosphere*. 2021;2021(Special 3). <https://doi.org/10.2113/2021/8684428>.
- Auradou H, Drazer G, Hulin JP, Koplik J. Permeability anisotropy induced by the shear displacement of rough fracture walls. *Water Resour Res*. 2005;41(9). <https://doi.org/10.1029/2005WR003938>.
- Li W, Wang Z, Qiao L, Yang J, Li J. Representative elementary surface for morphology and permeability of natural rock fractures. *Bull Eng Geol Env*. 2023;82(5):159. <https://doi.org/10.1007/s10064-023-03184-6>.
- Marchand S, Mersch O, Selzer M, et al. A stochastic study of flow anisotropy and channelling in open rough fractures. *Rock Mech Rock Eng*. 2020;53(1):233–249. <https://doi.org/10.1007/s00603-019-01907-4>.
- Jiang Z, Deng T, Yin Q, He L. Numerical modeling of fluid flowing properties through porous media with single rough fractures. *Geofluids*. 2021;2021, 6611723. <https://doi.org/10.1155/2021/6611723>.

49. Zou L, Ivars DM, Larsson J, Selroos J-O, Cvetkovic V. Impact of shear displacement on advective transport in a laboratory-scale fracture. *Geomech Energy Environ*. 2022; 31, 100278. <https://doi.org/10.1016/j.gete.2021.100278>.
50. Zhong Z, Wang L, Song L, et al. Size effect on the hydraulic behavior of fluid flow through a single rough-walled fracture. *Soil Dyn Earthq Eng*. 2021;143, 106615. <https://doi.org/10.1016/j.soildyn.2021.106615>.
51. Liu G, Zhao Z, Chen Y, Ma F, Wang G. Comparison between typical numerical models for fluid flow and heat transfer through single rock fractures. *Comput Geotech*. 2021;138, 104341. <https://doi.org/10.1016/j.compgeo.2021.104341>.
52. Zhong Z, Ding J, Hu Y. Size effect on the hydraulic behavior of fluid flow through rough-walled fractures: a case of radial flow. *Hydrogeol J*. 2022;30(1):97–109. <https://doi.org/10.1007/s10040-021-02415-y>.
53. Witherspoon PA, Amick CH, Gale JE, Iwai K. Observations of a potential size effect in experimental determination of the hydraulic properties of fractures. *Water Resour Res*. 1979;15(5):1142–1146. <https://doi.org/10.1029/WR015i005p01142>.
54. Neuzil CE, Tracy JV. Flow through fractures. *Water Resour Res*. 1981;17(1):191–199. <https://doi.org/10.1029/WR017i001p0191>.
55. Tsang YW, Witherspoon PA. The dependence of fracture mechanical and fluid flow properties on fracture roughness and sample size. *J Geophys Res Solid Earth*. 1983;88 (B3):2359–2366. <https://doi.org/10.1029/JB088iB03p02359>.
56. Méheust Y, Schmittbuhl J. Scale effects related to flow in rough fractures. *Pure Appl Geophys*. 2003;160(5):1023–1050. <https://doi.org/10.1007/PL00012559>.
57. Matsuki K, Chida Y, Sakaguchi K, Glover PWJ. Size effect on aperture and permeability of a fracture as estimated in large synthetic fractures. *Int J Rock Mech Min Sci*. 2006;43(5):726–755. <https://doi.org/10.1016/j.ijrmms.2005.12.001>.
58. Singh KK, Singh DN, Gamage RP. Effect of sample size on the fluid flow through a single fractured granitoid. *J Rock Mech Geotech*. 2016;8(3):329–340. <https://doi.org/10.1016/j.jrmge.2015.12.004>.
59. Karimzade E, Baghbanan A, Rahmani Shahraki A. Effects of fracture intersection on the hydraulic properties of 3D crossed rough-walled fractures. *Eng Geol*. 2023;314, 106997. <https://doi.org/10.1016/j.enggeo.2023.106997>.
60. Zhong Z, Xu C, Zhang F, Wang X, Hu Y. Size effect on hydraulic properties of rough-walled fractures upscaled from meter-scale granite fractures. *Geomech Geophys Geo-Energy Geo-Resour*. 2023;9(1):75. <https://doi.org/10.1007/s40948-023-00606-3>.
61. Ullman S, Brenner S. The interpretation of structure from motion. *Proc Roy Soc London Ser B Biol Sci*. 1997;203(1153):405–426. <https://doi.org/10.1098/rspb.1979.0006>.
62. Snavely N, Seitz SM, Szeliski R. *Photo tourism: exploring photo collections in 3D. Special Interest Group on Computer Graphics and Interactive Techniques Conference*. New York NY United States: Association for Computing Machinery; 2006. <https://doi.org/10.1145/1179352.1141964>. Boston, Massachusetts.
63. *CapturingReality. RealityCapture 1.2.1. Epic Games Slovakia*. 116295 ed. 2022.
64. Kimball S, Mattis P. *GIMP 2.10. 32 ed*. 2022.
65. Torkan M, Janiszewski M, Uotinen L, Baghbanan A, Rinne M. High-resolution photogrammetry to measure physical aperture of two separated rock fracture surfaces. *J Rock Mech Geotech Eng*. 2023. <https://doi.org/10.1016/j.jrmge.2023.10.003>.
66. Girardeau-Montaut D. *CloudCompare: 3D Point Cloud and Mesh Processing Software 2. 2022*, 6.1.
67. Li Y, Zhang Y. Quantitative estimation of joint roughness coefficient using statistical parameters. *Int J Rock Mech Min Sci*. 2015;77:27–35. <https://doi.org/10.1016/j.ijrmms.2015.03.016>.
68. Myers NO. Characterization of surface roughness. *Wear*. 1962;5(3):182–189. [https://doi.org/10.1016/0043-1648\(62\)90002-9](https://doi.org/10.1016/0043-1648(62)90002-9).
69. Yu X, Vayssade B. Joint profiles and their roughness parameters. *Int J Rock Mech Min Sci Geomech Abstr*. 1991;28(4):333–336. [https://doi.org/10.1016/0148-9062\(91\)90598-G](https://doi.org/10.1016/0148-9062(91)90598-G).
70. Zimmerman RW, Al-Yaarubi A, Pain CC, Grattoni CA. Non-linear regimes of fluid flow in rock fractures. *Int J Rock Mech Min Sci*. 2004;41(3):384. <https://doi.org/10.1016/j.ijrmms.2003.12.045>.
71. Moutsopoulos KN. Exact and approximate analytical solutions for unsteady fully developed turbulent flow in porous media and fractures for time dependent boundary conditions. *J Hydrol*. 2009;369(1):78–89. <https://doi.org/10.1016/j.jhydrol.2009.02.025>.
72. Torkan M, Uotinen L, Nieminen V, Rinne M. Photogrammetry based characterization of hydro-mechanical properties of a rock fracture. *IOP Conf Ser Earth Environ Sci*. 2021;833(1), 012019. <https://doi.org/10.1088/1755-1315/833/1/012019>.
73. *COMSOLAB. COMSOL Multiphysics® V. 6.1*. 2022. Stockholm, Sweden.
74. Uotinen L, Torkan M, Baghbanan A, Hernández EC, Rinne M. Photogrammetric prediction of rock fracture properties and validation with metric shear tests. *Geosciences*. 2021;11. <https://doi.org/10.3390/geosciences11070293>.
75. Torkan M, Janiszewski M, Uotinen L, Rinne M, Baghbanan A. Numerical study of scale effect on fluid flow through a rough fracture. *EUROCK*. 2024. <https://doi.org/10.1201/9781003429234-72>. Alicante, Spain; 2024.